

Coupled hydrologic-electromagnetic framework to model permafrost active layer organic soil dielectric properties



Kazem Bakian-Dogaheh ^{a,*}, Yuhuan Zhao ^a, John S. Kimball ^b, Mahta Moghaddam ^a

^a Department of Electrical and Computer Engineering, University of Southern California, Los Angeles, CA, USA

^b Numerical Terradynamic Simulation Group, W.A. Franke College of Forestry & Conservation, University of Montana, Missoula, MT, USA

ARTICLE INFO

Edited by Jing M. Chen

Keywords:

Dielectric measurement
Dielectric mixture model
Organic soil
Permafrost
Active layer

ABSTRACT

Arctic permafrost soils contain a vast reservoir of soil organic carbon (SOC) vulnerable to increasing mobilization and decomposition from polar warming and permafrost thaw. How these SOC stocks are responding to global warming is uncertain, partly due to a lack of information on the distribution and status of SOC over vast Arctic landscapes. Soil moisture and organic matter vary substantially over the short vertical distance of the permafrost active layer. The hydrological properties of this seasonally thawed soil layer provide insights for understanding the dielectric behavior of water inside the soil matrix, which is key for developing more effective physics-based radar remote sensing retrieval algorithms for large-scale mapping of SOC. This study provides a coupled hydrologic-electromagnetic framework to model the frequency-dependent dielectric behavior of active layer organic soil. For the first time, we present joint measurement and modeling of the water matric potential, dielectric permittivity, and basic physical properties of 66 soil samples collected across the Alaskan Arctic tundra. The matric potential measurement allows for estimating the soil water retention curve, which helps determine the relaxation time through the Eyring equation. The estimated relaxation time of water molecules in soil is then used in the Debye model to predict the water dielectric behavior in soil. A multi-phase dielectric mixing model is applied to incorporate the contribution of various soil components. The resulting organic soil dielectric model accepts saturation water fraction, organic matter content, mineral texture, temperature, and microwave frequency as inputs to calculate the effective soil dielectric characteristic. The developed dielectric model was validated against lab-measured dielectric data for all soil samples and exhibited robust accuracy. We further validated the dielectric model against field-measured dielectric profiles acquired from five sites on the Alaskan North Slope. Model behavior was also compared against other existing dielectric models, and an in-depth discussion on their validity and limitations in permafrost soils is given. The resulting organic soil dielectric model was then integrated with a multi-layer electromagnetic scattering forward model to simulate radar backscatter under a range of soil profile conditions and model parameters. The results indicate that low frequency (P-, L-band) polarimetric synthetic aperture radars (SARs) have the potential to map water and carbon characteristics in permafrost active layer soils using physics-based radar retrieval algorithms.

1. Introduction

In the past several decades, rising temperatures in the northern high latitudes (NHL) have played a primary role in altering ecosystem dynamics of the Arctic regions. Permafrost, or perennially frozen soil, is among the dominant subsurface features in the NHL Arctic tundra biome. As Arctic warming unfolds at more than three times the mean global warming rate, the vulnerability of soil organic matter exposed by permafrost thaw and the deepening of the active layer needs to be studied on a synoptic basis. To that end, the NASA Arctic Boreal

Vulnerability Experiment (ABoVE) was designed and is conducting a decadal campaign to study the Arctic ecosystem through an integrated field and airborne observations, which capture a wide bio-geophysical gradient (Miller et al., 2019; Kasischke et al., 2014). Airborne science, particularly the use of long wavelength P- and L-band (430 MHz – 1.26 GHz) radar instruments, plays a key role in the ABoVE campaign because microwave remote sensing has shown the potential to capture and monitor surface and subsurface properties in the Arctic relating to permafrost at various spatial and temporal scales (Smith et al., 2022; Stow et al., 2004). Dielectric mixing models for soils are the critical

* Corresponding author.

E-mail address: bakiando@usc.edu (K. Bakian-Dogaheh).

component in developing physics-based computational algorithms for retrieving soil moisture and soil organic matter based on radar or radiometer data obtained from airborne and spaceborne microwave sensors (Yi et al., 2022; Mironov et al., 2017). The lack of a well-established soil organic dielectric model limits the capabilities of radar retrieval algorithms for mapping the subsurface water and carbon characteristics in the permafrost landscape (Bakian-Dogaheh et al. (2022)). This work takes a comprehensive look at the current state of the problem by addressing the challenges of previous organic soil dielectric models and provides insights from measurement and modeling perspectives. Consequently, a new organic soil dielectric model is developed via detailed joint measurements and modeling of hydrological and dielectric properties of the permafrost active layer soils in Alaska.

1.1. Current state of the problem: measurement perspective

Characterizing the dielectric behavior of soil is a mature field of study and dates back to the early 1980s (Dobson et al., 1985; Hallikainen et al., 1985; Topp et al., 1980). However, those early efforts were mainly focused on mineral soils. Studying the dielectric characteristics of highly organic soils (histosols), typical of the Arctic permafrost active layer, has gained increasing attention more recently and especially within the last

decade. **Table 1** summarizes, to the best of our knowledge, the existing soil dielectric measurements reported in the literature that contain organic matter content. The measurements are categorized into in-situ (field) observations or lab-driven experiments. The field measurements are usually done by vertical insertion of a probe or opening a soil pit and horizontal insertion of the probe in each soil layer. The probes utilized in the field campaigns often operate in two manners: either based on time domain reflectometry (TDR) generating a wideband pulse, or frequency domain capacitive probes that operate at a single frequency of around 100 MHz or lower. Soil core samples are usually extracted for gravimetric soil moisture measurements along with detailed texture analysis to characterize the organic and mineral fractions (Park et al., 2021; Bakian-Dogaheh et al., 2020; Gnatowski et al., 2018; Bircher et al., 2016a; Manns and Berg, 2014; Rowlandson et al., 2013). In **Table 1**, only the work that simultaneously includes dielectric constant, soil moisture, and soil texture data was reported. Field measurements provide snapshot-type information and can be limited by other underlying factors, such as weather-related soil moisture variability. However, lab measurements provide a controlled environment where soil dielectric properties can be measured with greater precision over a full range of soil moisture conditions by either systematically drying or wetting a soil sample. Furthermore, the variety of instruments

Table 1

The current state of the problem from a measurement perspective and description of existing soil dielectric measurement data containing organic matter samples. Point refers to a pair of soil moisture (θ) and dielectric permittivity (ϵ) measurements (ϵ, θ). Soil moisture and dielectric properties can be obtained from respective soil gravimetric and probing measurements acquired during a field campaign. Sample refers to a “soil sample” under test in a controlled environment e.g., laboratory. Sample measurements are usually conducted over the entire range of soil moisture conditions, which results in multiple points (pair of ϵ, θ) from saturation to completely dry.

Paper	No. of Sample	OM [g/g] %	θ [cm ³ /cm ³] [0–0.8]	Frequency [MHz] NA**	Temperature [°C] NA	ϵ [-] ϵ'_r	Measurement Method TDR	Type Lab	Notes
Malicki et al. (1996)	62	[0–95] *	[0–0.8]	NA**	NA	ϵ'_r	TDR	Lab	Samples were sieved with 2-mm mesh, and packed before measurement
Gnatowski et al. (2018)	278 Points	[81–86] ***	[0.25–0.85]	NA	NA	ϵ'_r	TDR	Field	
Bircher et al. (2016a)	7	[31–93]	[0–0.9]	70	NA	ϵ_a	5TE Probe	Lab	ϵ_a : Apparent permittivity
	5	[5–15]		100		ϵ_a	Theta Probe		
Bircher et al. (2016b)	9	[51–98]	[0–0.85]	1260	20	$\epsilon'_r + i\epsilon''_r$	Resonant Cavity	Lab	
Mironov et al. (2015); Mironov et al. (2010)	5	[3–10]	[0–0.5]			$\epsilon'_r + i\epsilon''_r$	Coaxial waveguide (Transmission line)	Lab	Samples were dried and then ground with a coffee grinder. Technique applied for mineral soil.
Mironov and Savin (2015)	1	[80–90]	[0–0.6]	1400 [1000–16,000]	[-30 – +25]	$\epsilon'_r + i\epsilon''_r$			
	1	50	[0–0.4]	[50–15,000]	[-30 – +25]	$\epsilon'_r + i\epsilon''_r$			
Mironov et al. (2019)	5	[35–80]	[0–0.5]	1400	[-30 – +25]	$\epsilon'_r + i\epsilon''_r$			
Savin et al. (2020, 2022)	7	[35–90]	[0–0.6]	[10–15,000] 435	[-30 – +25]	$\epsilon'_r + i\epsilon''_r$			
Park et al. (2019)	15	[0–3]	[0–0.6]	30	20	$\epsilon'_r + i\epsilon''_r$	No new measurement	Lab	Literature Based
	9	25		30					
	8	[5–69]		100					
	1	0.6		1000					
Park et al. (2021)	702 Points	[0–10]	[0–0.6]	50	NA	ϵ'_r	Hydra Probe	Field	Rowlandson et al. (2013); Manns and Berg (2014)
Liu et al. (2013)	12	[0–18]	[0–0.6]	[50–40,000]	23	$\epsilon'_r + i\epsilon''_r$	Coaxial Probe	Lab	
Bakian-Dogaheh et al. (2020); Bakian-Dogaheh et al. (2022)	144 Points	[2–100]	[0–0.95]	70	[5–15]	$\epsilon'_r + i\epsilon''_r$	TEROS 12 Probe	Field	
This work	66	[2–100]	[0–0.95]	70	22.5	$\epsilon'_r + i\epsilon''_r$	TEROS 12 Probe	Lab	

* In the paper, the organic carbon (OC) is reported, herein we used OM = 1.72 × OC.

** Not Available.

*** In the paper, the ash (AC) content is reported, herein we used OM = 100-AC

for lab experiments is more diverse, and reportedly coaxial probes, waveguides, resonant cavities, or dielectric probes have been used for dielectric characterization (Savin et al., 2020, 2022; Mironov et al., 2019; Mironov and Savin, 2015; Mironov et al., 2015; Mironov et al., 2010; Bircher et al., 2016b). The lab measurement instruments often use a vector network analyzer that can potentially enable a wide frequency response characterization of soil dielectric up to 15GHz, particularly using coaxial probes and coaxial waveguides.

The existing challenges in the reported organic soil dielectric measurement in the literature could be studied from various aspects. Initially and from a textural analysis standpoint, the majority of in-lab measurements are conducted over a small number of samples that only contain an extreme range of organic matter (OM) contents. In other words, the soil samples are either highly organic or highly mineral with minimal OM content. The limited number of samples and associated limited OM range leads to large uncertainty in OM models developed and validated based on these samples, particularly for an area such as

the Arctic, which encompasses a wide range of soil texture variability. Additionally, the measurement methods utilized for in-lab characterization are often destructive. For example, one study reported that soil samples were ground with a coffee grinder to make them homogenized for filling the coaxial container (Mironov et al., 2017). This is primarily due to measurement techniques that are more suitable for homogenized samples, such as mineral soils, which have fundamentally different physical properties than organic soils. These destructive measurement methods are likely to change the physics of more heterogeneous organic soils by disturbing the pore distribution of soil particles. Consequently, as shown in Table 1, the range of soil saturation (porosity) is often limited to a range [e.g., 0–0.6 m³/m³], whereas in reality, a much higher range of saturation is expected for organic soils (in Table 1, compare Bircher et al., 2016a and Mironov et al., 2019). Lastly, and from a practical standpoint, state-of-the-art land surface remote sensing radar instruments often operate at a lower frequency range of the microwave spectrum, particularly at P- or L-bands (Chapin et al., 2012; Rosen et al.,

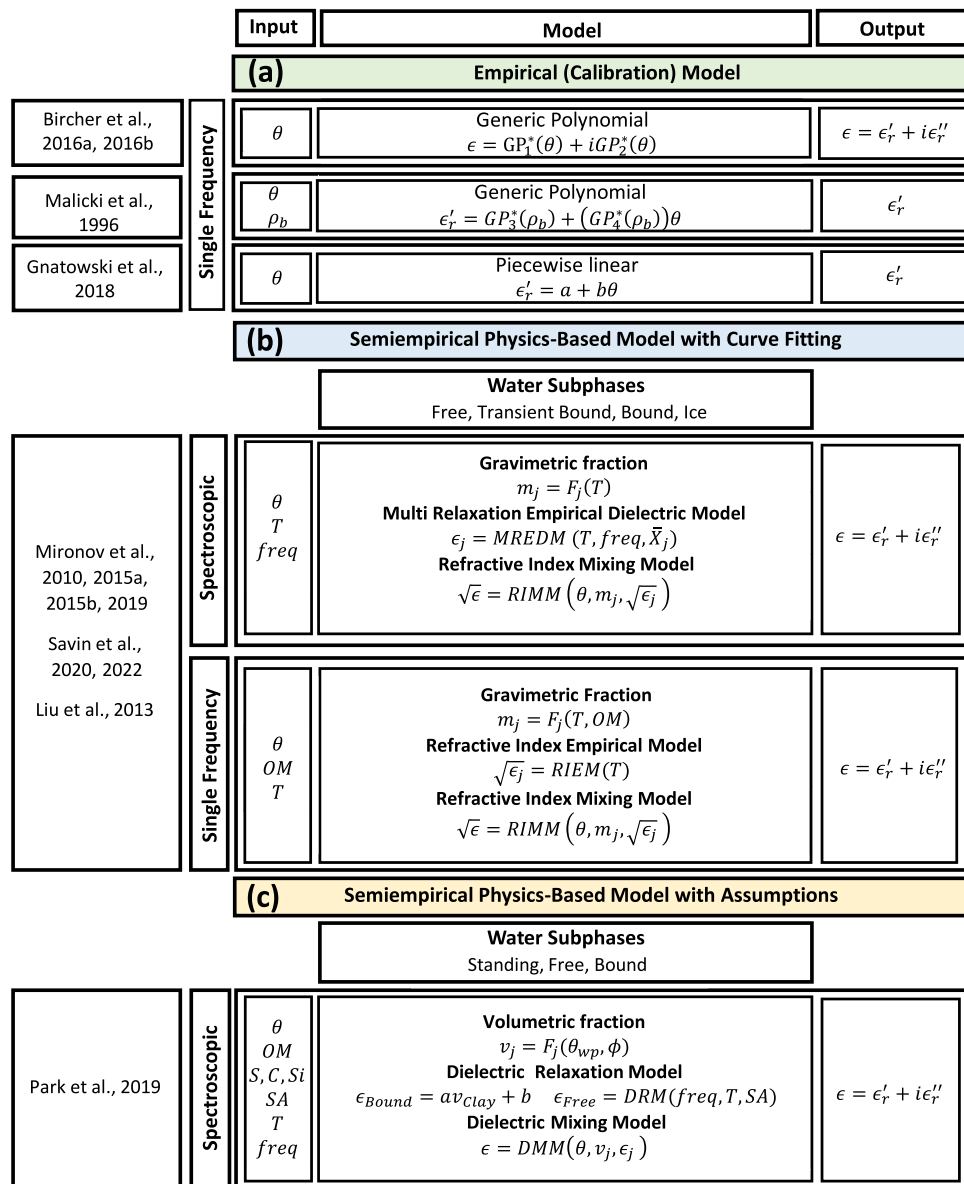


Fig. 1. The current state of the problem from a modeling perspective. A description of existing organic soil dielectric models, including: (a) empirical models that relate soil dielectric permittivity to soil moisture through a generic polynomial; (b) the semiempirical physics-based model developed by Mironov et al. and consisting of a spectroscopic and single-frequency approach, where organic matter serves as a model input; (c) the semiempirical physics-based model developed by Park et al. that relies on wilting point as a proxy measure of bound water.

2006). Therefore, a wideband frequency response of soil up to 15GHz is not expected to be utilized in remote sensing of soil profiles and adds more complexity when dealing with highly heterogeneous and porous organic soil.

1.2. Current state of the problem: modeling perspective

The early development of soil dielectric models focused on mineral soils. The availability of new organic soil dielectric datasets in recent years has enabled a few organic soil dielectric modeling studies, which can be broadly categorized into three main types (Fig. 1). Initially, empirical (calibration) models were used to describe simple relationships between soil moisture and measured dielectric permittivity (Bircher et al., 2016a, 2016b). While most of these calibration equations are generic polynomial functions without including soil physical information, a few models reported multivariable frameworks that, besides soil moisture, include other soil properties such as bulk density as inputs (Malicki et al., 1996). The significance of finding a relationship between soil dielectric and soil bulk density is inherently due to the strong correlation of bulk density to soil texture, particularly with OM content (Bakian-Dogaheh et al., 2020). The second category of organic soil dielectric models was adapted from the original work of Mironov et al. (2004) for mineral soil dielectric modeling, which treats water in soil as having multiple phases. Through a semi-empirical physics-based model, the dielectric behavior and fraction of water subphases are found based on fitting the water dielectric behavior parameters to the measured soil dielectric permittivity (Mironov et al., 2010; Mironov et al., 2015; Mironov and Savin, 2015; Mironov et al., 2019; Savin et al., 2020, 2022; Liu et al., 2013). Two sub-categories of this model include a spectroscopic model and a single-frequency approach. The spectroscopic model was based on a single soil sample, which accepts soil moisture (θ), temperature, and frequency as inputs and arrives at the bound, free, transient bound water and ice dielectric properties through multi-relaxation empirical dielectric models (MREDM) along with their associated fractions. The single-frequency approach, however, accepts OM content along with temperature and soil moisture as input parameters. The last category of organic soil dielectric models is similar to the semi-empirical physics-based approach but relies on certain hydrological assumptions to arrive at the bound water fraction. In this method, bound water fraction is associated with the permanent wilting point, and bound water dielectric properties are treated as a variable to fit the measured soil dielectric properties (Park et al., 2019, 2021).

A physics-based radar retrieval algorithm, particularly for permafrost active layer soil, requires a physics-based organic soil dielectric model that - in the most general form- accepts soil moisture (θ), organic matter (OM), sand (S) and clay (C) fractions, temperature (T), and microwave frequency (freq) as inputs and arrives at the equivalent complex dielectric permittivity of the soil sample. A main idea in the physics-based modeling framework is to rely on the fundamental soil properties that govern other physical properties of soil. For instance, bulk density (ρ_b) and soil porosity (ϕ) both can be derived from OM and mineral texture. Therefore, a generic calibration-based model, in which often-times only the real part of the dielectric (relative permittivity) is found through a polynomial function of soil moisture, won't be applicable. While the semi-empirical physics-based models such as Mironov et al. (2017) have introduced major advances in the area of organic soil dielectric modeling, for a more complete representation of arctic soils, we need models that can represent the physical construct of the soil matrix, the full range of soil moisture values, and the full range of organic matter content. Lastly, Park et al. (2019) proposed a new avenue of organic soil dielectric modeling by associating the bound water fraction in soil to the permanent wilting point. However, the initial parametrization of this model is based on Jin et al. (2017), and Yang et al. (2014) in which the OM variation is constrained to a lower range that doesn't capture the wide variety of arctic soil conditions (a more detailed analysis is provided in the discussion section 4.3–4.4).

1.3. Remaining major challenges

The above literature review reveals two major challenges for a reliable organic soil dielectric model development: 1) a more realistic approach to model the dielectric behavior of water inside the soil matrix, and 2) a detailed set of dielectric measurements for a wide range of organic matter to achieve a more comprehensive model validation is needed. Characterizing the behavior of water-in-soil has been a challenging open problem in the field of soil dielectric mixture modeling. Historically, water in the soil would be treated as a discrete multiphase system composed of bound and free water fractions. Oftentimes, the amount and dielectric properties of bound water would conveniently serve as fitting parameters to match with measurements and soil dielectric model predictions (Dyck et al., 2019). Bound water generally refers to the first few layers of water molecules adjacent to soil particles and is correlated with the specific surface area (SSA) of soil particles (Peplinski et al., 1995). Over the past few decades, a number of approaches have been proposed for determining the amount of bound water volumetric fraction and estimating its dielectric properties. For example, some models suggested the relaxation time of bound water molecules, and the associated volumetric fraction can be found as a function of distance from soil particles, in which the distance is related to the soil bulk density and SSA (Or and Wraith, 1999; Boyarskii et al., 2002; Schwartz et al., 2009a, 2009b). While specific surface area has been shown as an essential parameter that governs the physical and chemical properties of porous media, a well-established relationship between SSA and general soil physical properties is required for soil dielectric modeling. Particularly for Arctic organic soil, the basic information of soil physical properties, along with a comprehensive SSA characterization, are very sparse. Petersen et al. (1996) showed that SSA is highly correlated to water-in-soil content at -1500 kPa. In the water-in-soil retention curve, this pressure is known as the permanent wilting point, where plants are no longer able to overcome the adsorption force between solid soil particles and water molecules. Accordingly, this provided a new promise in soil dielectric modeling, in which the wilting point (θ_{wp}) has been assumed as a proxy measure for determining the bound water fraction in soil (Park et al., 2017, 2019).

While the importance of determining dielectric properties for different water subphases (bound and free) is apparent in governing soil dielectric permittivity, some other studies note the additional importance of other parameters such as structural configuration, bulk density, and porosity (Friedman, 1998; Jones and Friedman, 2000; Robinson and Friedman, 2001; Cosenza and Tabbagh, 2004). Overall, there has been debate on the contribution of "bound" water to govern the (water content – permittivity) relationship in soil compared to the "microstructure" and "phase configuration" that is governed by inter/intra aggregate pores (Blonquist Jr et al., 2006; Robinson et al., 2009; Dyck et al., 2019). The boundary between inter/intra aggregate pores could be determined using the hydraulic critical water content (θ_{hc}) calculated from the soil water retention curve (SWRC). Accordingly, at θ_{hc} a change in dielectric response is expected.

Whether the changes in soil dielectric properties at lower soil moisture levels could be associated with the critical water content (θ_{hc}), or permanent wilting points (θ_{wp}) a sufficient understanding of water dielectric properties inside soil still remains unknown, due to the lack of a direct measurement method. Regardless, the hydrological properties of soil in the form of soil water retention curves have been shown to be important for determining the soil dielectric permittivity. Additionally, other studies have suggested another approach in dealing with water dielectric properties in soil. Hilhorst et al. (2001) suggested that water-in-soil should be treated as a continuous phase, where the Debye relaxation model can predict its dielectric permittivity. Accordingly, the relaxation time of water-in-soil molecules can be found from the Gibbs free energy enthalpy through the Eyring equations, where the Gibbs energy is associated with soil matric potential. While this approach

shows promise toward establishing a universal organic-mineral soil dielectric model, it has not been widely verified and experimentally investigated, and it has only been studied for very limited mineral soil conditions (Wagner and Scheuermann, 2009).

1.4. New set of dielectric and matric potential measurement and modeling

The significance of using a soil water retention curve in modeling water-in-soil dielectric permittivity goes beyond soil dielectric modeling and can potentially synergize the modeling activities of electromagnetic and hydrology communities. However, a detailed soil measurement is needed to explore the validity of this model experimentally. To that end, a total of 66 soil samples were harvested from 9 sites within the North Slope and interior Alaska (Fig. 2). Five sites were located within the North Slope including Franklin Bluffs (FB), Sagwon (SGW), Happy Valley (HV), Ice Cut (ICC), and Innavaait Creek (IMN). The sites in interior Alaska include Eight Mile Lake (EML), Creamers Field (CF), Ballaine Road (BR), and Scottie Creek (SC). Sampling locations fall within airborne SAR transects from the NASA ABoVE Airborne Campaign (AAC). Samples were carefully extracted from 12 soil pits and were shipped to the University of Southern California for further analysis. A comprehensive soil characterization was conducted that included measuring dielectric, matric potential, and volumetric soil moisture for

all soil samples. Furthermore, a detailed soil texture analysis was performed to fully characterize the physical properties of soil samples, such as total organic matter, root biomass, soil organic matter, bulk density, porosity, and fiber content (Bakian-Dogaheh et al., 2023). These measurements form the basis for the model development and validation in this paper. We used a soil dielectric probe (METER TEROS 12), which measures the dielectric permittivity and electrical conductivity at 70 MHz, and a TEROS 21 porous disk probe for measuring soil matric potential; a complete description of the measurements is discussed in the following method section (TEROS 12 manual, TEROS 21 manual).

The work presented here is comprised of both hydrology and electromagnetic perspectives. The hydrology part of this work is presented in another study (Bakian-Dogaheh, In Prep.), where the volumetric fraction of soil constituents including root biomass (RB), soil organic matter (SOM), and mineral (Min) content, are used to derive the parameters of soil water retention curve model. This paper presents the remaining work, where the method section addresses the complete end-to-end coupled hydrologic-electromagnetic (Hydro-EM) model. A detailed description of soil dielectric, matric potential, and other soil physical properties derived from laboratory analysis is provided, which serve as the main validation dataset for the model assessment along with additional in-situ soil profile characterization as ancillary validation. The methods also include discussion on the implication of the organic

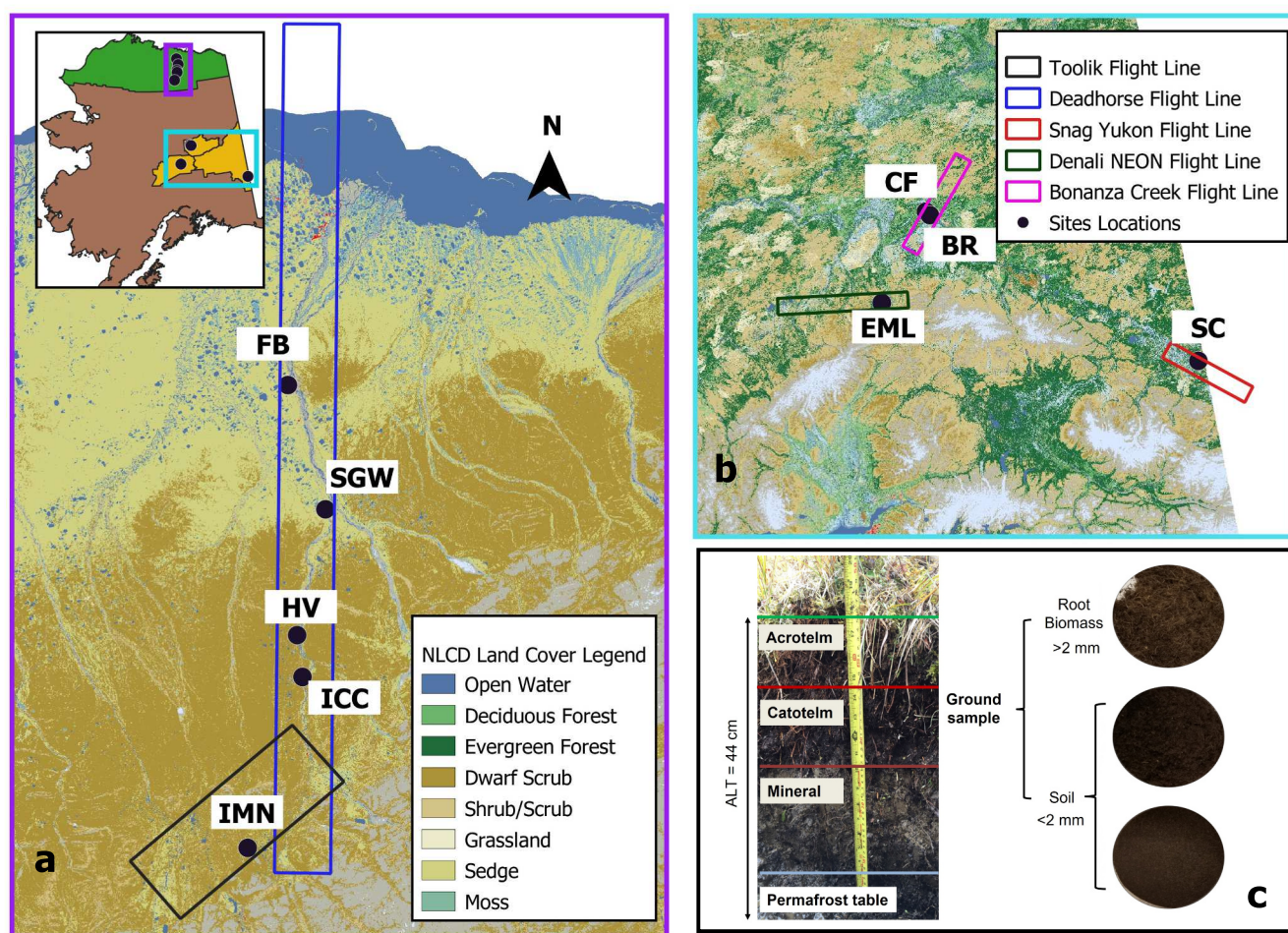


Fig. 2. Locations of our nine study sites and associated land cover types across Alaska. The Alaskan North Slope, and interior Alaska regions are indicated by the green and yellow shades, respectively, in the inset in (a). The purple and cyan boxes around (a) and (b) correspond to the same colour boxes in the inset map, respectively. Black dots in (a) and (b) show the site locations where soil samples were collected and analyzed for determining soil characteristics and laboratory analysis. Sampling locations fall within airborne SAR transects from the NASA ABoVE airborne campaign. (c) An example soil profile from an excavated pit, where active layer samples were harvested from the surface to permafrost table. (For interpretation of the references to colour in this figure legend, the reader is referred to the web version of this article.)

soil dielectric model in physics-based radar remote sensing. The results section analyzes the organic soil dielectric model performance in estimating soil dielectric properties against laboratory and in-situ measurements. Various discussion points are then elaborated to clarify the requirements of empirical modeling, organic soil dielectric model behavior at different frequencies and temperatures. Additionally, an intercomparison between the new and existing organic soil dielectric models, and the limitations of our proposed model is addressed in the discussion section. Finally, the importance of the new soil dielectric model is demonstrated by integrating it into a physics-based radar retrieval algorithm to investigate the feasibility of the model for retrieving water and carbon characteristics of the active layer, which is paramount to determining SOC vulnerability in Arctic permafrost landscapes.

2. Method

2.1. Coupled hydro-EM approach for soil dielectric modeling

The framework of an end-to-end Hydro-EM approach for modeling the dielectric properties of organic soil aims to arrive at a model that relates the input parameters including soil moisture, organic matter, mineral texture, temperature, and frequency to the organic soil dielectric behavior (Fig. 3). The framework consists of a hydrology perspective, from which one can determine the soil water retention curve of a given soil sample through a detailed model parameterization scheme, using basic soil physical properties such as root biomass, soil organic matter, and mineral fraction. The Eyring equation bridges the hydrology and electromagnetic components of the framework by relating the estimated soil water retention curve to predict the water relaxation time in soil, which can then be applied to a Debye relaxation model to determine the water-in-soil dielectric properties. Finally, the resulting water dielectric properties are inserted into a dielectric mixing model, where the contribution of water and other subphases in soil are taken

into account to arrive at the effective dielectric behavior of the organic soil samples.

2.1.1. Water-in-soil dielectric model

A detailed soil model parameterization scheme was developed from the hydrology perspective, which aims to model the soil water retention curve (SWRC) parameters. In this work, we present a summary of the parameterization scheme for the Campbell water retention curve, while a more detailed parameterization description is provided elsewhere (Bakian-Dogaheh, In Prep.).

The Campbell SWRC relates the soil saturation fraction (SW) and soil matric potential (ψ_m) through an exponential model for non-saturated zones (Campbell, 1974):

$$\psi_m = \psi_s(SW)^{-b} [kPa] \quad (1a)$$

$$SW = \frac{\theta}{\phi} [cm^3/cm^3] \quad (1b)$$

where, the Campbell model parameters include air entry potential (ψ_s) and the exponent parameter (b). Soil saturation fraction (SW), can be found as the normalized ratio of soil moisture (θ) with respect to maximum saturation or porosity (ϕ). The Campbell model parameterization developed in our previous work suggests that ψ_s and b can be derived from the contribution of three main solid components of the soil: root biomass (RB), soil organic matter (SOM), and mineral fraction (Min). The total organic matter (OM) as shown in Eq. (2) consists of RB, which refers to all organic matter larger than 2 mm in diameter, and SOM, which refers to organic matter less than 2 mm in size (Compare ground sample, RB and SOM in Fig. 2.c). While technically, the soils refer to materials existing in a ground sample that are less than 2 mm in diameter, throughout this paper, we use ground and soil alternatively. Additionally, mineral fraction refers to the mineral parts of the soil particles that are determined through hydrometer methods for the samples and include sand (S), silt (Si), and clay (C) fractions.

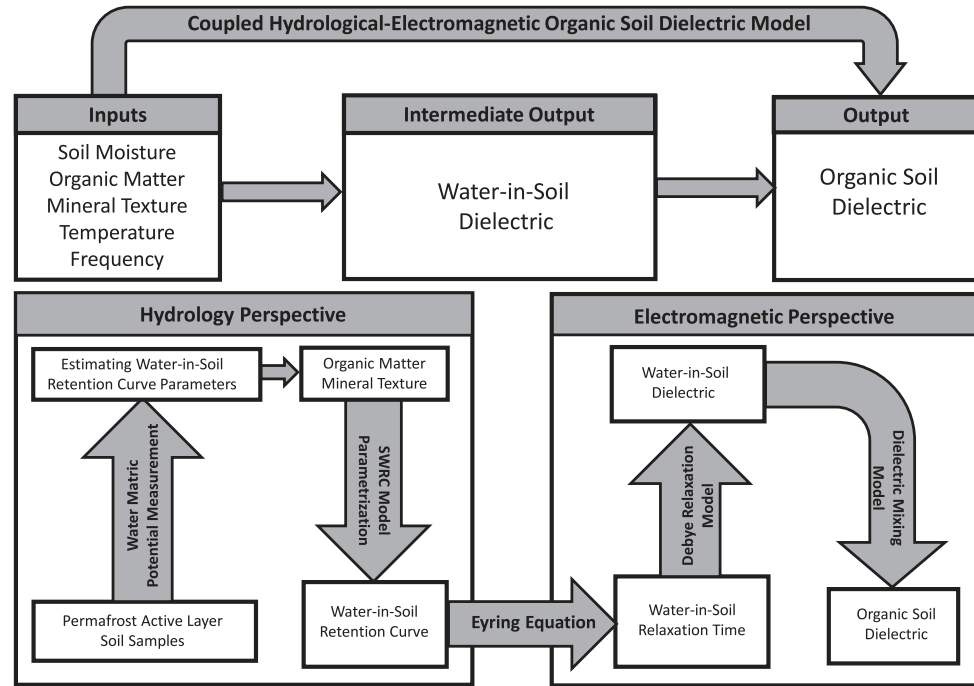


Fig. 3. The end-to-end coupled hydrologic-electromagnetic organic soil dielectric model aims to use basic soil properties (including soil moisture, organic matter, mineral texture, temperature, and frequency) as input parameters to determine the effective soil dielectric of the soil sample. The model consists of a hydrology perspective that parametrizes the soil water retention curve using various inputs. The electromagnetic perspective relates the estimated soil water retention curve to the soil water relaxation time using the Eyring equation and arrives at the water-in-soil dielectric condition using the Debye dielectric model. Finally, the resulting water-in-soil dielectric is applied to the organic soil dielectric mixing model along with other subphases to calculate the organic soil dielectric properties.

$$OM = RB + (1 - RB) \times SOM \text{ [g/g]} \quad (2)$$

While RB and SOM are the independent variables for characterizing organic properties of soil (ground) samples, based on detailed soil physical properties measurements we developed empirical equations to determine these properties along with other soil properties such as bulk density (ρ_b), specific bulk density (ρ_s), and porosity (ϕ) as a function of OM, which varies between [0–1] [g/g].

$$RB = 0.0016 \times e^{6.393 \times OM} \text{ [g/g]} \quad (3a)$$

$$SOM = 0.9164 \times OM + 0.003 \text{ [g/g]} \quad (3b)$$

$$\rho_b = e^{-3.143 \times OM + 0.564 \times S + 0.8134 \times C} \text{ [g/cm}^3\text{]} \quad (3c)$$

$$\rho_s = -1.535 \times OM + 2.3656 \text{ [g/cm}^3\text{]} \quad (3d)$$

$$\phi = -0.3733 \times \rho_b + 0.9282 \text{ [cm}^3/\text{cm}^3\text{]} \quad (3e)$$

In Eq. (3), bulk density was expressed as a function of total organic matter (OM), and the percentage of sand (S) and clay (C) in soil (Notice the difference between hydrometer measurement output and mass fraction calculation). Accordingly, the mass fraction for each of the solid components can be found through the following equations:

$$f_m^{RB} = RB \text{ [g/g]} \quad (4a)$$

$$f_m^{SOM} = (1 - RB) \times SOM \text{ [g/g]} \quad (4b)$$

$$f_m^{Min} = (1 - RB) \times (1 - SOM) \text{ [g/g]} \quad (4c)$$

$$f_m^S = S \times f_m^{Min} \text{ [g/g]} \quad (4d)$$

$$f_m^C = C \times f_m^{Min} \text{ [g/g]} \quad (4e)$$

$$f_m^{Si} = Si \times f_m^{Min} \text{ [g/g]} \quad (4f)$$

Note that in determining mass fractions, we assumed the soil samples are gravel (rock, pebble) free. The volumetric fraction (f_v^i) of each sub-component denoted with $i = \{RB, SOM, \text{ or } Min\}$, and can be found by incorporating the specific density (ρ_s^i) of each element into the corresponding mass fraction (f_m^i) and bulk density (ρ_b).

$$f_v^i = f_m^i \times \frac{\rho_b}{\rho_s^i} \text{ [cm}^3/\text{cm}^3\text{]} \quad (5a)$$

$$\tilde{f}_v^i = \frac{f_v^i}{1 - \phi} \text{ [-]} \quad (5b)$$

We use $OM = \{0, 0.7, 1\}$ as designators of pure mineral, soil organic matter, and root biomass fractions, respectively. Therefore, the corresponding specific density of RB, SOM, Min, can be found as follows: $\{\rho_s^{RB} = 0.8306, \rho_s^{SOM} = 1.29, \rho_s^{Min} = 2.36\}$. Accordingly, we use Eq. (5b) to normalize the volumetric fraction of each sub-component to the total pore space fraction, which determines the contribution of solid sub-components of soil samples in deriving the SWRC model parameters as follows:

$$\psi_s = (\psi_s^{Min})\tilde{f}_v^{Min} + (58.52)\tilde{f}_v^{SOM} + (28.63)\tilde{f}_v^{RB} \text{ [cm]} \quad (6a)$$

$$b = (b_{Min})\tilde{f}_v^{Min} \times (1.82)\tilde{f}_v^{SOM} \times (0.22)\tilde{f}_v^{RB} \text{ [-]} \quad (6b)$$

The coefficients in Eq. (6) are adapted from Bakian-Dogaheh et al., (In Prep). Additionally, the mineral soil contribution can be expressed using the following empirical relationship:

$$\psi_s^{Min} = 10^{(-1.31 \times S + 1.8799)} \quad (7a)$$

$$b^{Min} = 16.1 \times C + 2.8266 \quad (7b)$$

where S and C are sand and clay fractions, respectively, and vary between [0–1] [g/g].

Eqs. (2–7) enable the complete reconstruction of the Campbell soil water retention curve. The SWRC model parameters were simulated for an average soil consisting of 36 % sand and 25 % clay as well as for all different classes of mineral soil (all class types) over the full OM range of [0–100] [g/g] %, shown as the shaded area in Fig. 4. Once the SWRC is fully characterized, the water-in-soil dielectric can be predicted by incorporating the SWRC into the Eyring equation to find the relaxation time of water-in-soil, and finally by applying the relaxation time into Debye relaxation model.

$$\epsilon_W = \epsilon_{W\infty} + \frac{1}{\theta} \int_0^\theta \left(\frac{\epsilon_{W0} - \epsilon_{W\infty}}{1 - i2\pi \times freq \times \tau_W} \right) d\theta + i \frac{\sigma_W}{2\pi\epsilon_0 \times freq} \text{ [-]} \quad (8)$$

where ϵ_{W0} [–] is the static dielectric constant (at $freq = 0$), the high-frequency dielectric constant (as $freq \rightarrow \infty$) is denoted by $\epsilon_{W\infty}$ [–], the relaxation time is described by τ_W [s], electrical conductivity is described by $\sigma_W \left[\frac{S}{m} \right]$, and ϵ_0 is the free space permittivity.

Buchner et al. (1999) proposed that the relaxation time of water-in-soil (τ_w) is directly connected to the corresponding average number of hydrogen bonds, which must be broken to achieve ‘mobile’ water molecules that are able to re-orient with the applied electromagnetic field. Arrhenius equations with temperature independent parameters fail to capture the connection of τ_w to the kinetics of the hydrogen-bond network. Therefore, the characteristic feature of τ_w with nonlinear temperature dependence of its activation energy, suggests that $\tau_w(T)$ should be modeled by an Eyring approach with a temperature-dependent free energy of activation (ΔG_w^*) (Buchner et al., 1999, Wagner and Scheuermann, 2009).

In Eq. (8) the water-in-soil relaxation time (τ_w) can be expressed by the Eyring equation as:

$$\tau_w = \frac{h}{k_B(T + 273.15)} e^{\frac{\Delta G_0^*(T) + |\psi_m(\theta)|V}{R(T + 273.15)}} \text{ [s]} \quad (9)$$

where h and k_B are the Planck and Boltzmann constants, T is the soil temperature in Celsius (°C), R is the ideal gas constant, and θ is the soil moisture. The difference between the Gibbs energy of free water molecules (ΔG_0^* [J]) and water molecules inside the soil matrix (ΔG_w^*) is related to the soil matric potential ($\psi_m(\theta)$ [kPa]), where $V = 18.07 \times 10^{-6}$ [m³/mol] is the molar volumetric fraction of water. By incorporating Eq. (9) into Eq. (8), we can find the equivalent water-in-soil dielectric properties. The remaining Debye relaxation parameters ($\epsilon_{W\infty}$, ϵ_{W0} , and τ_0) are assumed to be equal to that of “free-water” and are adapted from Ulaby et al. (2014). Similar assumptions have been made in other studies such as Dyck et al. (2019), where the lower and upper frequency Debye parameter was substituted by existing “free-water” models. Finally, the water-in-soil electrical conductivity (σ_W) was modeled empirically as a function of soil mineral texture (see discussion section).

$$\epsilon_{W0} = 88.045 - 0.415 \times T + 6.29 \times 10^{-4} \times T^2 + 1.07 \times 10^{-5} \times T^3 \text{ [-]} \quad (10a)$$

$$\epsilon_{W\infty} = 4.9 \text{ [-]} \quad (10b)$$

$$\tau_0 = \left(\frac{1}{2\pi} \right) \times (1.1109 \times 10^{-10} - 3.824 \times 10^{-12} \times T + 6.938 \times 10^{-14} \times T^2 - 5.096 \times 10^{-16} \times T^3) \text{ [s]} \quad (10c)$$

$$\Delta G_0^* = \ln \left(\frac{\tau_0 \times (T + 273.15) \times k_B}{h} \right) \times (R \times (T + 273.15)) \text{ [J]} \quad (10d)$$

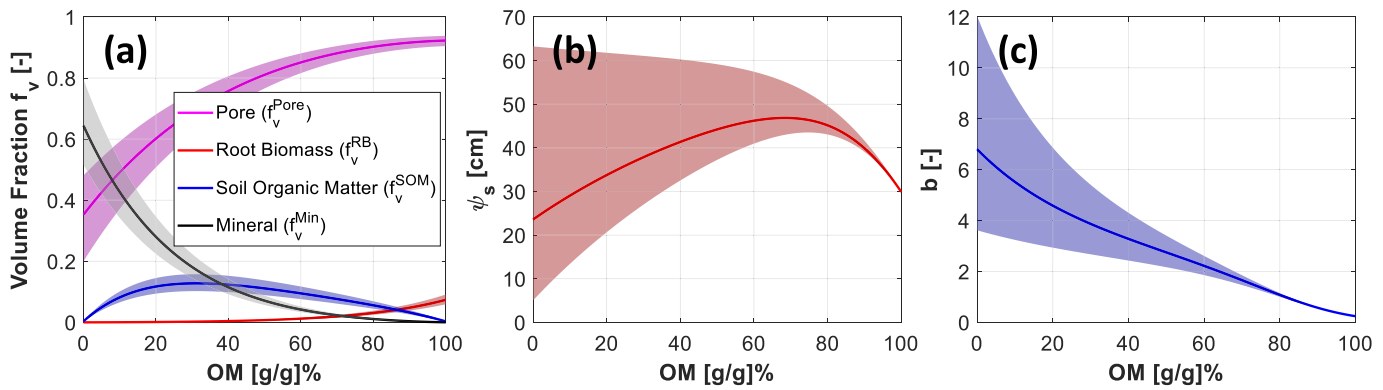


Fig. 4. In all cases, the solid lines are derived from the model simulation for a fraction of $S = 36\%$ and $C = 25\%$ as OM varies between $[0 - 100]$ [g/g]%, and the shaded areas are associated with the total range of variation simulated for all classes of mineral soil. (a) Shows the volumetric fractions of solid soil components (solid plot), which includes root biomass, soil organic matter, and mineral soil, and the porosity along with their associated variation (shaded) as the model presented in Eq. (2–5) simulated different classes of mineral soil. (b) Shows the variation of air entry potential (ψ_s) of Campbell SWRC model parameters. (c) The behavior of exponent parameters of the Campbell SWRC and its associated variation.

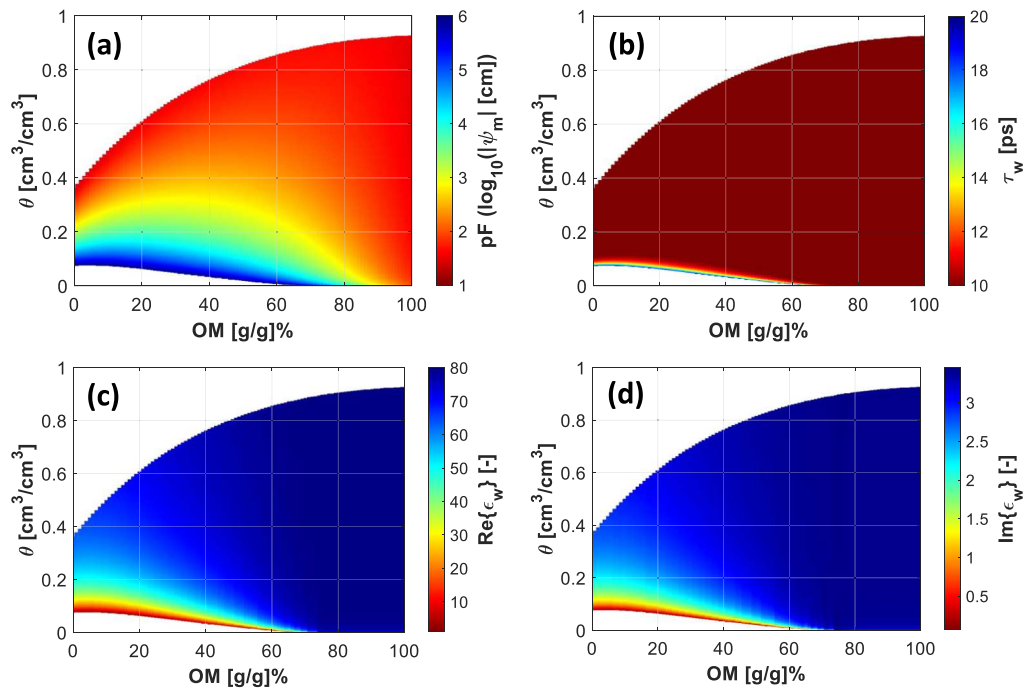


Fig. 5. The full simulation of the hydrology perspective for the full range of soil moisture and organic matter content for an average mineral texture with $S = 36\%$ and $C = 25\%$. (a) Shows variation of soil matric potential $pF = \log_{10}|\psi_m|$. (b) Relaxation time of water molecules in soils. (c) Real part of water-in-soil dielectric permittivity. (d) Imaginary part of water-in-soil dielectric permittivity.

The full simulation of the model is shown in Fig. 5. For a typical mineral soil that contains 36 % sand and 25 % clay, the soil water retention curve was simulated for the full range of saturation and OM content (Fig. 5a). Subsequently, the relaxation time is calculated by incorporating the SWRC into the Eyring equation. Results reveal that the variation of the relaxation time only exhibits non-free water behavior at the lower end of soil moisture content compared to the overall free-water type behavior of water in the soil for the majority of the range at higher soil moisture levels (Fig. 5b). Finally, the real and imaginary parts of the water-in-soil dielectric are plotted for the variation of soil moisture and OM (Fig. 5c-5d).

Throughout the manuscript the matric potential (ψ_m) or air entry potential (ψ_s) is alternatively represented with kPa or cm units using the following conversion: $1 \text{ [kPa]} \approx 10.19 \text{ [cm]}$ of water.

2.1.2. Freeze/thaw state

The temperature varies substantially within the permafrost active layer, and across the profile the heat flux determines whether the water-in-soil is frozen or thawed (Fuchs et al., 1978). When the soil temperature reaches the freezing temperature (T_f), not all water-in-soil will be frozen. In winter, the active layer can experience soil temperatures below -10°C , with about 8 % and 6 % of volumetric soil moisture remaining unfrozen in the mineral and organic soil layers, respectively (Hinzman et al., 1991).

The amount of unfrozen and frozen water content in the soil matrix should be characterized before incorporating the water dielectric behavior contribution into the dielectric mixing model. Over the past decades and for fully saturated soils, many approximations have been proposed to estimate the unfrozen water content in soil (also known as supercooled liquid soil water), including a power law function

($V_w^{UnFrozen} = A|T|^{-B}$) described by Romanovsky and Osterkamp (2000).

Niu and Yang (2006), which are the basis for freeze/thaw modeling for Land Surface Models such as the Community Land Model-5 (CLM 5 documentation, n.d), describe super cooled soil water at subfreezing temperatures according to a depression in freezing point. When ice forms in the soil matrix, the water matric potential (ψ_m) and vapor pressure over pure ice reach equilibrium (Mölders et al., 2003). Fuchs et al. (1978) expressed ψ_m as a function of latent heat (L_f) and soil temperature (T) in degree Celsius:

$$\psi_m = \frac{L_f(T_f - T)}{g(T + 273.15)} \quad (11)$$

where $L_f = 333000 \left[\frac{J}{kg} \right]$, and $g = 9.82 \left[\frac{m}{s^2} \right]$ is the gravitational constant.

The volumetric frozen water content (V_w^{Frozen}) is calculated based on the difference between total water within the soil and the maximum liquid water ($V_w^{UnFrozen}$) content below freezing temperature (T_f):

$$V_w^{total} = \frac{\rho_w^{Frozen}}{\rho_w^{UnFrozen}} \times V_w^{Frozen} + V_w^{UnFrozen} \quad (12)$$

In Eq. (12), $\rho_w^{Frozen} = 917 \left[\frac{kg}{m^3} \right]$ refers to ice density and $\rho_w^{UnFrozen} = 1000 \left[\frac{kg}{m^3} \right]$ is the liquid water content.

By equating eqs. (11) and (1), which describes the soil water matric potential of liquid water, we can derive the freezing-point depression equation, which can be used to determine the upper limit of the unfrozen water content at subfreezing temperature:

$$V_w^{UnFrozen} = \begin{cases} \phi & T \geq T_f \\ \phi \left[100 \times \frac{L_f}{g\psi_s} \frac{(T_f - T)}{(T + 273.15)} \right]^{-\frac{1}{b}} & T < T_f \end{cases} \quad (13)$$

where the ψ_s [cm] and b [–] as described previously are the Campbell SWRC parameters. The freezing temperature (T_f) in general is governed by soil physical properties and can be estimated through various methods such as variational data assimilation (Nicolksy et al., 2009). In this work and for simplicity we follow the CLM-5 assumptions and assume $T_f = 0$ [°C].

While Eq. (12) is potentially applicable to the full range of soil saturation, for the sake of model simplicity and in the case of permafrost active layer soil, to find the V_w^{Frozen} , we assume that the soil in the vicinity of frozen water table is saturated:

$$V_w^{Frozen} = \frac{\rho_w^{UnFrozen}}{\rho_w^{Frozen}} \times (\phi - V_w^{UnFrozen}) \quad (14)$$

It is important to note that Eqs. (13–14) only work for below freezing temperatures, and for thawed soil we still use Eq. (1). The model simulation for a representative tundra soil sample (OM = 80 %, S = 36 %, C = 25 %) shows the behavior of frozen and unfrozen water content for different subzero temperatures, where the model exhibits an increase in total volume of water under subzero temperatures (Fig. 6).

2.1.3. Dielectric mixing model

Once the water-in-soil dielectric properties are characterized, and the freeze/thaw state is determined, the contribution of soil constituents can be incorporated into the dielectric mixing model. Historically, various soil dielectric mixing models have been suggested for mineral soil dielectric models (e.g., Ulaby et al., 2014). In this work, we utilize a simplified version that is based on the volumetric fraction mixing by suggesting an empirical exponent power term (α). The term α varies between [0.3–1] [–] and was found for each soil sample based on the soil physical properties (discussion section).

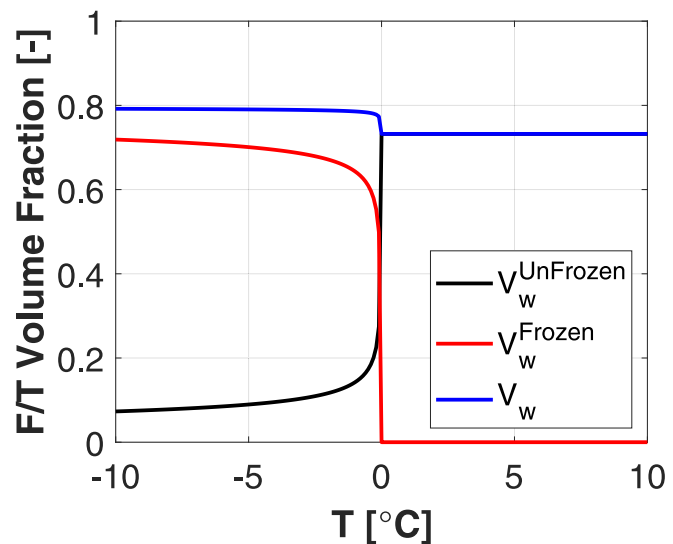


Fig. 6. The simulation of freeze/thaw state, and volumetric fraction behavior of water and ice content as temperature varies from sub-zero to above zero conditions for a representative soil sample (OM = 80 %, S = 36 %, C = 25 %). While the OM + S + C summation can exceed 100 % based on the equations provided in (4-a to 4-f), $f_m^{OM} + f_m^S + f_m^C + f_m^{SI} = 100\%$ and differentiates the mass fraction of the entire sample compared to the measured sand/clay soil fractions from hydrometer method.

$$\epsilon_{soil} = \begin{cases} \left(f_v^{Min} \epsilon_{Min}^\alpha + f_v^{OM} \epsilon_{OM}^\alpha + f_v^W \epsilon_W^\alpha + f_v^A \epsilon_A^\alpha \right)^{\frac{1}{\alpha}} & T \geq T_f \\ \left(f_v^{Min} \epsilon_{Min}^\alpha + f_v^{OM} \epsilon_{OM}^\alpha + f_v^{UnFW} \epsilon_W^\alpha + f_v^I \epsilon_I^\alpha \right)^{\frac{1}{\alpha}} & T < T_f \end{cases} \quad (15)$$

The dielectric constant of solid subcomponents usually shows negligible dispersion (no sensitivity to frequency) and is determined from the literature. Accordingly, for mineral soil, organic soil, and frozen water (ice) components we use $\epsilon_{Min} = 4.7$, $\epsilon_{OM} = 1.7$, and $\epsilon_I = 3.17$, respectively (Ulaby et al., 1990; Ulaby and El-Rayes, 1987; Matzler and Wegmüller, 1987; Dobson et al., 1985).

As stated above, for frozen soil, the volumetric frozen and unfrozen water content are found based on the assumption that the soil is saturated. Therefore, the pore space is only filled with unfrozen water and ice. In other words, for above-zero [°C] temperature, Eq. (15) works for the whole range of saturation, whereas the mixing model at subzero temperatures is only valid for saturated soil as described in Eq. (13–14). The total volumetric fraction behavior of each subcomponent can be described as:

$$\begin{cases} f_v^W + f_v^A + f_v^{Min} + f_v^{OM} = 1 & T \geq T_f \\ f_v^{UnFW} + f_v^I + f_v^{Min} + f_v^{OM} = 1 \rightarrow \begin{cases} f_v^I = V_w^{Frozen} & T < T_f \\ f_v^{UnFW} = V_w^{UnFrozen} & T > T_f \end{cases} & T < T_f \end{cases} \quad (16)$$

2.2. Soil dielectric and soil matric potential measurement

The soil samples collected for laboratory measurements exhibit a relatively uniform distribution for low OM content (below 20 %, No. 26), and higher OM (above 60 %, No. 32), whereas the mid-range of organic matter content (between 20 and 60 %) is less represented in our samples (Fig. 7). Soil samples were collected from 12 sampling points at 8 locations in the Alaskan North Slope and 4 locations in Interior Alaska. At each sampling point, samples were collected at various depths through the active layer profile. A brief summary of soil properties collected is provided in Table 2, along with a full description of the samples in the associated dataset (Bakian-Dogaheh et al., 2023). Notice,

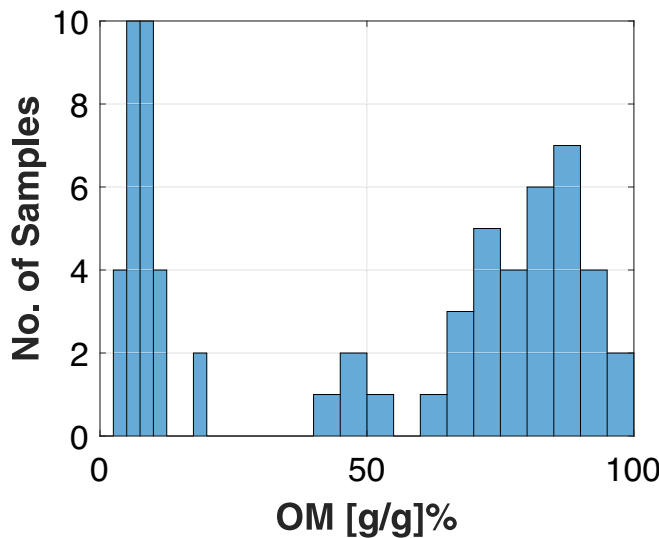


Fig. 7. The organic matter (OM) content histogram distribution of the Alaska samples used in the laboratory analysis for characterizing the soil dielectric and matric potential.

for the top soil, due to minimal presence of mineral soil the measurements of soil mineral texture were not applicable (shown with dash).

2.2.1. Soil dielectric measurement

The soil dielectric measurement was conducted using METER TEROS 12 capacitive dielectric probes ([TEROS 12 manual](#)). The TEROS 12 probe consists of 3 needles, which enable measuring the raw analog to digital converter (ADC) value as an indicator of real part of the soil complex permittivity (needles 1–2), the measurement of electrical conductivity (σ) that helps characterize the imaginary part ($\epsilon_r'' = \frac{\sigma}{2\pi\epsilon_0 f_0}$) of the soil complex dielectric permittivity (needles 2–3), and a thermistor (needle 2) that measures the soil temperature ([Fig. 8a](#)). The soil measurements were conducted in the laboratory at an ambient temperature ($\sim 22^\circ\text{C}$).

The sensors were inserted into the soil layer horizontally, and brought to oversaturation. Once the excess water was evaporated, the measurement started as the sample dried down ([Fig. 8b,d–e](#)). At each measurement point (soil moisture values), the raw ADC and electrical conductivity were recorded 20 times for redundancy. Furthermore, the saturation-drying process was repeated twice to ensure repeatability. The mean value for each measurement set (each sample consisting of 2 sets) was used for validation purposes.

The TEROS 12 sensors operate at 70 MHz and needles 1 and 2 measure raw ADC values derived from an internal algorithm to minimize the electrode polarization effect ([TEROS 12 manual](#)). To translate raw ADC to relative permittivity (real part of dielectric), usually one can refer to the manufacturer curve. However, as mentioned in the TEROS 12 user manual, the curve provided by the company was meant to map the raw ADC to the apparent permittivity (ϵ_a), which incorporates both real and imaginary parts of the permittivity ([Friedman, 1998](#); [Sihvola and Alanen, 1991](#)).

$$\epsilon_a = \epsilon' \left(\frac{1 + \sqrt{1 + \tan^2 \left(\frac{\epsilon'}{\epsilon''} \right)}}{2} \right) \quad (17)$$

Therefore, to calibrate the TEROS 12 sensors, we created several synthetic samples (a mixture of isopropyl and water) to capture the entire range of relative permittivity [1–80]. The Agilent 85070E Dielectric Probe Kit and a Vector Network Analyzer were used to measure the reference dielectric values for each sample. To study the variation among probes, a total of 9 TEROS 12 probes were used, with a total

of 45 measurements for each synthetic sample. Using a ProCheck data-logger and TEROS 12 probe, five measurement points were recorded for each sensor. Accordingly, a new calibration curve was constructed that enabled analysis of the accuracy of the provided calibration curve by METER ([Fig. 9](#)). While the overall behavior of the new calibration curve is very similar to the manufacturer, there is a slight underestimation between manufacturer curve compared with our measurement due to the differences between (ϵ_a) apparent and relative (ϵ') permittivity. Therefore, for the analysis in this paper, we used the calibration curve developed from the mean values of measurements in Eq. (18).

It is important to note that the nominal operating frequency of the Agilent Probe starts from 500 MHz, whereas the TEROS 12 sensor operates at 70 MHz. To calibrate the TEROS 12 sensors, we established a relationship between raw ADC values measured by the TEROS 12 and a reference dielectric mixture measured by the Agilent Probe. The frequency response for all of the dielectric mixtures is relatively flat, exhibiting negligible dispersion. Therefore, we assumed the frequency response for the dielectric mixture behavior at 70 MHz to be similar to those measured at 500 MHz using the Agilent Probe.

$$\epsilon_r' = (2.2 \times 10^{-9} \text{ADC}^3 - 1.48 \times 10^{-5} \text{ADC}^2 + 0.035 \times \text{ADC} - 27.25)^2 \quad (18)$$

2.2.2. Soil matric potential

The details of the soil matric potential measurement have been reported in [Bakian-Dogaheh et al. \(2023\)](#). Here we present a summary of the measurement procedure. To measure the soil water matric potential, the TEROS-21 sensor uses a solid matrix equilibration technique, which is achieved by introducing a ceramic disk with known pore size distribution into soil and allowing the material to reach hydraulic equilibrium ([Fig. 8c](#)). At equilibrium, measuring the water potential of the solid matrix of the porous ceramic disk gives the soil water matric potential. The operation of the TEROS-21 sensor is agnostic to the soil type as long as the hydraulic equilibrium and sufficient hydraulic connectivity are satisfied according to Second Law of Thermodynamics ([TEROS 21 manual](#)).

To determine the water potential of the solid matrix (porous ceramic disk), the TEROS-21 measures the dielectric permittivity of the solid matrix. The dielectric permittivity of the porous ceramic disk is substantially dependent on the moisture content in the pore spaces. The TEROS-21 measures the permittivity of the porous disk, which in-turn can be translated into moisture level. Such techniques do not impose any requirements for further calibration and are agnostic to soil-type since the relationship between the engineered porous ceramic disk water content and permittivity are well established and are dependent on the pore space permittivity ($\epsilon_{\text{Ceramic}}$), and the amount of air (ϵ_{Air}) and water (ϵ_{Water}) in the ceramic pore spaces.

$$\epsilon_{\text{Porous Ceramic Disk}} = \text{function}(\epsilon_{\text{Water}}, \epsilon_{\text{Ceramic}}, \epsilon_{\text{Air}}) \quad (19)$$

The water potential is inferred from the water content of the porous disk through the water characteristics (retention) curve of the engineered porous disk. The total soil water potential (ψ_t) of the solid matrix can be written from the various subcomponents including pressure (ψ_p), gravitational (ψ_g), osmotic (ψ_o), and matric (ψ_m) potentials as follows:

$$\psi_t = \psi_p + \psi_g + \psi_o + \psi_m \quad (20)$$

For the TEROS-21 probe, the first three terms (ψ_p, ψ_g, ψ_o) are negligible, and only matric potential is influenced by the forces and attraction of water molecules to soil particles, which is the dominant element in the total soil water potential. Therefore, in effect the TEROS-21 measures the soil water matric potential.

The main shortcoming of the porous disk method is the range of measurement, which is limited by the distribution and size of the pore spaces in the ceramic disk. Additionally, the measurement at low moisture levels may be less accurate; although, the manufacturer

Table 2

Summary of soil samples collected from the North Slope and Interior of Alaska. The complete detailed soil physical properties are reported in the associated dataset from Bakian-Dogaheh et al. (2023). Dashes refer to measurements that are not applicable, due to minimal presence of mineral soil.

No.	Site Name	Soil ID	Depth [cm]	Mineral Soil type	Location	Soil Texture [g/g] %			
						Organic Matter	Sand	Silt	Clay
North Slope of Alaska									
1		FB-1-1	[0–7.5]	Sandy Loam		12.3	58.5	20.5	21
2		FB-1-2	[7.5–15]	Sandy Loam		9.8	64	17	19
3		FB-1-3	[15–22]	Sandy Clay Loam		6.7	62.5	16.5	21
4		FB-1-4	[22–29]	Sandy Loam	N 69° 48'44.54"	6.6	66.5	16.5	17
5	Franklin Bluffs	FB-1-5	[29–35.5]	Silt Loam	W 148° 45'59.35"	8.5	60	19	21
6		FB-1-6	[35.5–42]	Loam		7.2	50.5	30.5	19
7		FB-1-7	[42–48.5]	Sandy Clay Loam		4.7	53.5	24.5	22
8		FB-1-8	[48.5–55]	Loam		5.8	52.5	29.5	18
9		SGW-1-1	[0–8]	—		50.2	—	—	—
10		SGW-1-2	[8–16]	Sandy Loam		9.1	55	27	18
11		SGW-1-3	[16–23.5]	Sandy Clay Loam	N 69° 28'46.48"	5.4	52	26	22
12	Sagwon	SGW-1-4	[23.5–30]	Sandy Clay Loam	W 148° 33'51.99"	2.7	55	21	24
13		SGW-1-5	[30–37]	Sandy Clay Loam		2.8	52	21	27
14		SGW-1-6	[37–44]	Sandy Clay Loam		2.8	45	26	29
15		SGW-2-1	[0–6]	—		72.8	—	—	—
16		SGW-2-2	[6–12]	—		80	—	—	—
17		SGW-2-3	[12–17]	—		82	—	—	—
18	Sagwon	SGW-2-4	[17–22]	—	N 69° 28'35.68"	66.6	—	—	—
19		SGW-2-5	[22–27]	Clay Loam	W 148° 33'51.96"	48.8	23	46	31
20		SGW-2-6	[27–32]	Clay Loam		9.7	26	40	34
21		SGW-2-7	[32–37]	Clay		8.4	31	29	40
22		SGW-2-8	[37–42]	Clay Loam		8.9	26	39	40
23		HV-1-1	[0–7]	—		87.5	—	—	—
24		HV-1-2	[7–14]	Silty Clay Loam		17.6	20.5	59	20.5
25		HV-1-3	[14–19]	Silt Loam		11.1	17.5	53	29.5
26	Happy Valley	HV-1-4	[19–24]	Silt Loam		9	18.5	53	28.5
27		HV-1-5	[24–29]	Silty Clay Loam	N 69° 9'19.28"	7.2	14.5	56	29.5
28		HV-1-6	[29–34]	Silty Clay Loam	W 148° 50'19.64"	5.5	14.5	50	35.5
29		HV-1-7	[34–39]	Silty Clay Loam		6.1	14.5	50	35.5
30		HV-1-8	[39–44]	Silty Clay Loam		8.6	16.5	55.5	28
31		HV-2-1	[0–7.5]	—		93.5	—	—	—
32		HV-2-2	[7.5–15]	—	N 69° 9'19.29"	89.5	—	—	—
33	Happy Valley	HV-2-3	[15–22]	—	W 148° 50'30.48"	71.1	—	—	—
34		HV-2-4	[22–29]	Silt Loam		6.2	17	60	35.5
35		HV-2-5	[29–36]	Silt Loam		7.1	18	55.5	28
36		ICC-1-1	[0–7]	—	N 69° 2'30.82"	88.1	—	—	—
37	Ice Cut	ICC-1-2	[7–14]	—	W 148° 49'37.31"	76.3	—	—	—
38		ICC-1-3	[14–20]	Loam		17.7	28	49	23
39		ICC-1-4	[20–26]	Loam		10.4	28	50	22
40		ICC-1-5	[26–32]	Silt Loam		8.6	29	55	16
41		ICC-1-6	[32–38]	Silt Loam		10.7	33.5	49.5	17
42		ICC-2-1	[0–7]	—	N 69° 2'32.94"	83.3	—	—	—
43	Ice Cut	ICC-2-2	[7–14]	—	W 148° 49'31.38"	79.2	—	—	—
44		ICC-2-3	[14–20]	—		72.9	—	—	—
45		ICC-2-4	[20–26]	Loam		41.2	51.5	32	16.5
46		IMN-1-1	[0–7.5]	—	N 68° 36'17.90"	93.2	—	—	—
47		IMN-1-2	[7.5–15]	—	W 149° 18'22.86"	67.4	—	—	—
48	Imnavait Creek	IMN-1-3	[15–22]	—		74.3	—	—	—
49		IMN-1-4	[22–29]	—		61.4	—	—	—
50		IMN-1-5	[29–36]	Loam		7.8	44	31	25
Interior Alaska		CF-1-1	[0–5]	—		87	—	—	—
51		CF-1-2	[5–10]	—	N 64° 52'10.08"	85.8	—	—	—
52	Creamers Field	CF-1-3	[10–15]	—	W 147° 44'20.54"	84.9	—	—	—
53		CF-1-4	[15–20]	—		79	—	—	—
54		BR-1-1	[0–5]	—		92.8	—	—	—
55	Ballaine Road	BR-1-2	[5–10]	—	N 64° 54'54.00"	90.8	—	—	—
56		BR-1-3	[10–15]	—	W 147° 50'19.10"	82.1	—	—	—
57		BR-1-4	[15–20]	—		86.5	—	—	—
58		SC-1-1	[0–5]	—	N 62° 41'50.47"	74.2	—	—	—
59	Scottie Creek	SC-1-2	[5–10]	—	W 141° 8'32.40"	75.7	—	—	—
60		SC-1-3	[10–15]	—		65.2	—	—	—
61		SC-1-4	[15–20]	—		48.3	—	—	—
62		EML-1-1	[0–5]	—	N 63° 52'39.32"	100	—	—	—
63		EML-1-2	[5–10]	—	W 149° 15'20.70"	96.2	—	—	—
64	8-Mile Lake	EML-1-3	[10–15]	—		89.5	—	—	—
65		EML-1-4	[15–20]	—		81.2	—	—	—

guarantees accuracy down to wilting point (1500 kPa). Another challenge with the TEROS-21 is ensuring adequate hydraulic connectivity, particularly for highly organic soil; this was addressed by horizontally inserting the probe within the soil container and using multiple

redundant measurements at various soil moisture levels. While a more detailed description and discussion of the measurement is left to a forthcoming paper, we note that the major contribution of the soil matric potential measurement was to build a parametrization scheme

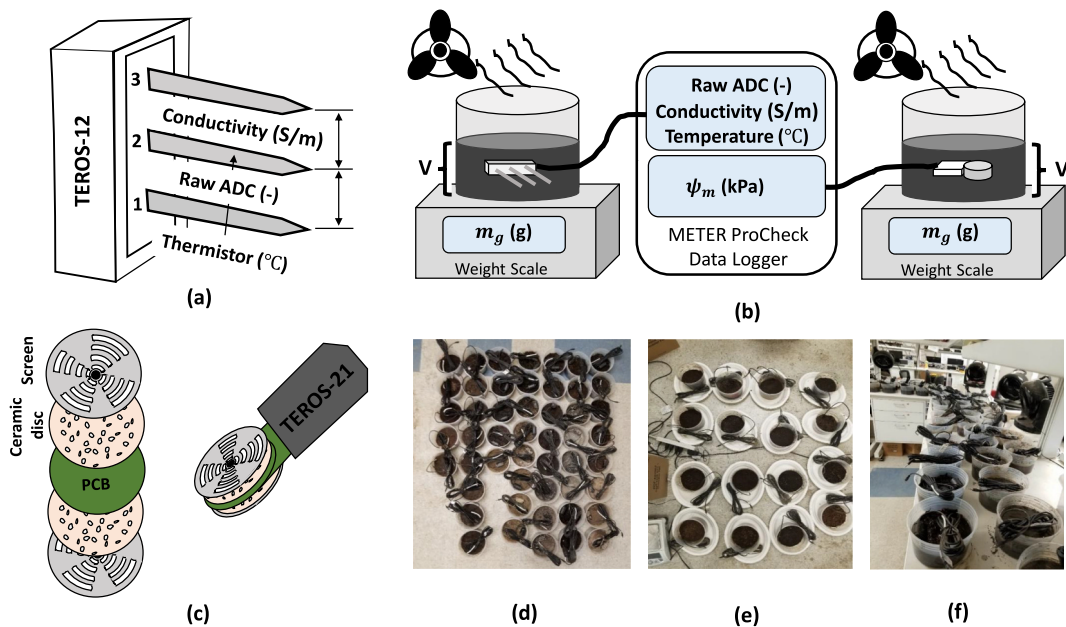


Fig. 8. (a) The TEROS 12 sensor enables raw ADC, conductivity and temperature measurements. (b) Schematic of soil dielectric and soil matric potential measurement set up, where sensors are inserted horizontally within the saturated soil layer. Measurement was conducted in a dry-down manner with the help of several fans that accelerated evaporation rates. (c) TEROS 21 sensor enabled soil matric potential measurement. (d) The batch of 50 samples that were collected from 8 sampling locations in the North Slope of Alaska. (e) A total of 16 soil samples from Interior Alaska were also collected. (f) Samples on the bench top in the vicinity of the fan used for air circulation.

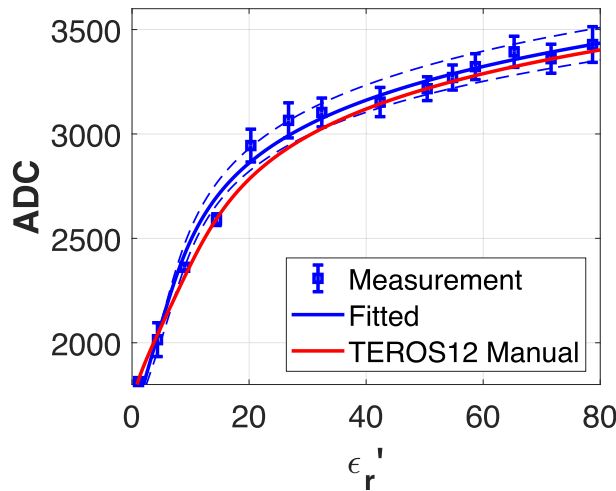


Fig. 9. The TEROS 12 manufacturer curve (red line) tends to slightly underestimate the relative permittivity of reference samples compared to the in-lab generated calibration curve (fitted blue line). The range of raw ADC values was generated by 45 measurements acquired from 9 TEROS 12 probes. The calibration curve was generated from the measured mean values. (For interpretation of the references to colour in this figure legend, the reader is referred to the web version of this article.)

for relatively poorly studied tundra organic soil, and this measurement has a significant influence on better understanding the soil hydraulic and thermal properties (Yi et al., 2018). The 66-soil water retention curves estimated from the measurement of soil matric potential (not shown here) were essential in developing Eqs. 6 and 7.

2.2.3. Soil moisture measurement

Each sample was brought to saturation by adding water to an overflow range. The samples were then left until excess water levels decreased to the soil surface as confirmed by visual inspection.

Accordingly, the volume of the saturated soil was then measured and marked on each container (Fig. 8b). The average volume of each sample was around ~ 950 [cm^3], comprising a container with diameter of 16 [cm], and filled to ~ 5 [cm] height. For each measurement point (soil moisture level), we recorded the mass of soil samples, including the container and sensor. The samples were under constant air flow generated by several fans, which were turned off for weight measurement (Fig. 8d). At each soil moisture level, the total mass of the container, sensors, and soil were measured to find the equivalent volumetric water content based on knowing the volume of the soil and the bulk density of the sample.

2.3. In-situ soil physical properties and dielectric profile measurement

In 2018, a comprehensive field survey was conducted on the North Slope of Alaska to characterize tundra active layer soil physical properties (organic matter, mineral texture, bulk density, and porosity) along with soil moisture and soil dielectric properties throughout the active layer profile. These measurements were acquired from eight soil pits at five sites. The set of in-situ soil moisture and dielectric permittivity measurements serves as an additional validation dataset in this work. Details regarding the various measurement procedures used in this study are described in Bakian-Dogaheh et al. (2022), while here the measurements are briefly summarized.

2.3.1. Soil physical properties

The field campaign was initially focused to collect a representative sample pool that helps to develop models to capture OM, SW, and T variation along the active layer profile (z). At each soil pit, two replicate samples with the interval of 5 [cm] were extracted from the side wall. The weight of the samples was measured in the field and samples were shipped to the laboratory for further analysis to determine in-situ soil saturation fraction bulk-density, porosity, OM content (Loss-on-Ignition), and soil mineral texture analysis using hydrometer methods.

The collective analysis of soil physical properties across the different soil pits resulted in developing models that capture the variation of fundamental surface and subsurface geophysical parameters including

OM, SW, and T along the active layer soil profile.

$$OM(z) = OM_{z0} + \frac{OM_M - OM_{z0}}{1 + e^{-\beta(z-z_{OLT})}} \quad (21a)$$

$$SW(z) = \begin{cases} 1 - (1 - SW_{z0}) \left(\frac{z}{z_{WT}} - 1 \right)^2 & z \geq z_{WT} \\ 1 & z < z_{WT} \end{cases} \quad (21b)$$

$$T(z) = T_{z0} \left(1 - \left(\frac{z}{z_{ALT}} \right)^2 \right) \quad (21c)$$

The organic matter profile model in Eq. (21a) consists of four parameters, including surface organic matter (OM_{z0}), and deep mineral organic matter (OM_M), along with an empirical shape factor (β) and the organic layer thickness (z_{OLT}). Two main parameters, surface saturation fractions (SW_{z0}) and water table depth (z_{WT}), govern the behavior of soil saturation profile. Finally, we modeled the temperature profile with a quadratic function, where (T_{z0}) represents the soil surface temperature, and (z_{ALT}) denotes the active layer thickness. We further assumed that the mineral fraction through the profile is constant and equal to the average value of the mineral layer.

$$S(z) = S_{avg} \quad (22a)$$

$$C(z) = S_{avg} \quad (22b)$$

Based on our modeling approach the contribution of mineral fractions for the highly organic soil model parametrization will be very small, since the mineral fraction is negligible. The range of measured parameters and associated model behavior for OM, S, C, SW, and T and their associated variations at each depth interval 5 [cm] through the profile is shown in Fig. 10 for all sites and sampling locations.

2.3.2. In-situ dielectric measurements

The soil dielectric measurements in the field were performed by inserting the TEROS-12 probes horizontally at the excavated side wall of each soil pit, where the measurement was conducted before soil sampling. The in-situ dielectric measurements were more detailed across the active layer profile with an interval depth of ~ 2.5 [cm]. Besides the soil dielectric measurement, which was adopted from the raw ADC measurement as described in section 2.2.1, the TEROS-12 probes also provided measurements of soil temperature and soil electrical conductivity.

This dielectric measurement was used to assess the estimated soil dielectric profile behavior, which was reconstructed using the organic soil dielectric model and the soil physical properties as model inputs as follows:

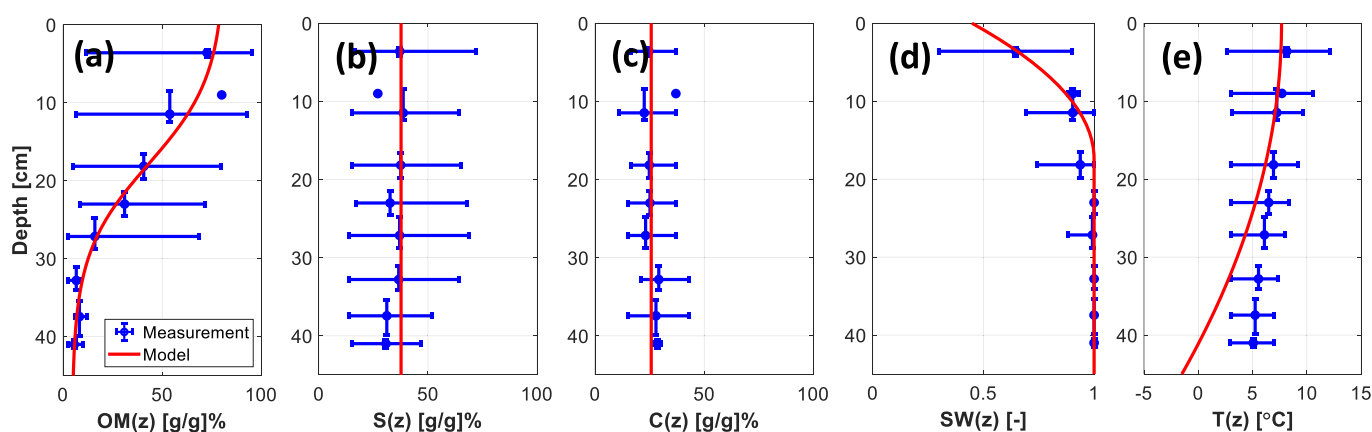


Fig. 10. The profile behaviors of the active layer soil properties that serve as input parameters for the soil dielectric model. (a) Organic matter content, (b-c) sand and clay fraction, (d) soil saturation fraction, and (e) temperature profile.

$$\epsilon_{soil}(z) = \epsilon'_{soil}(z) + i\epsilon''_{soil}(z) \quad (23a)$$

$$\epsilon_{soil}(z) = MODEL(OM(z), SW(z), T(z), S(z), C(z); freq) \quad (23b)$$

where the soil complex permittivity including real part (ϵ'_{soil}) and imaginary parts (ϵ''_{soil}) can be expressed through MODEL, which refers to the developed soil dielectric model in this work.

2.4. Role of organic soil dielectric model in physics-based radar remote sensing

The ultimate implication of an organic soil dielectric model is the integration of such model into a physics-based radar retrieval algorithm to estimate the permafrost active layer subsurface geophysical parameters (e.g., organic matter, soil-saturation, and temperature profiles). In forward-centric retrieval techniques, understanding the forward model is key (Akbar et al., 2017). The forward model consists of three main steps: 1) subsurface profile model, 2) soil dielectric model, and 3) electromagnetic scattering model. First, the geometry of the subsurface will be reconstructed by inserting the state parameters (\bar{X}_{STATE}) into the profile model. In the case of the permafrost active layer, the state parameters can be described as follows:

$$\bar{X}_{STATE} = \{OM_{z0}, z_{OLT}; SW_{z0}, z_{WT}; h, z_{ALT}\} \quad (24)$$

where the OM parameters including shape factor (β), and the deep organic matter (OM_M), were assumed to be constant (Bakian-Dogaheh et al., 2023). Furthermore, the (T_0, S_{avg}, C_{avg}) are assumed to be known. Once the profiles are reconstructed, they feed into Eq. (23) to arrive at the soil dielectric profile at the radar operating frequencies ($freq$). Then a layered dielectric structure is constructed (Fig. 11). Finally, this layered structure along with the surface roughness height (h), and the radar incidence angle (θ_{inc}) is fed into the electromagnetic scattering model that utilizes small perturbation method (SPM) to arrive at radar back-scattering coefficients (σ_{xx}) by (Tabatabaeenejad and Moghaddam, 2006).

$$\sigma_{xx} = SPM(\epsilon_{soil}(z), h, \theta_{inc}, Freq) \quad (25)$$

Where $xx : \{hh, vv\}$ denotes the horizontal and vertical co-polarized radar observations, respectively.

3. Results

3.1. Organic soil dielectric model validation in lab

The developed model was validated against both laboratory and in-

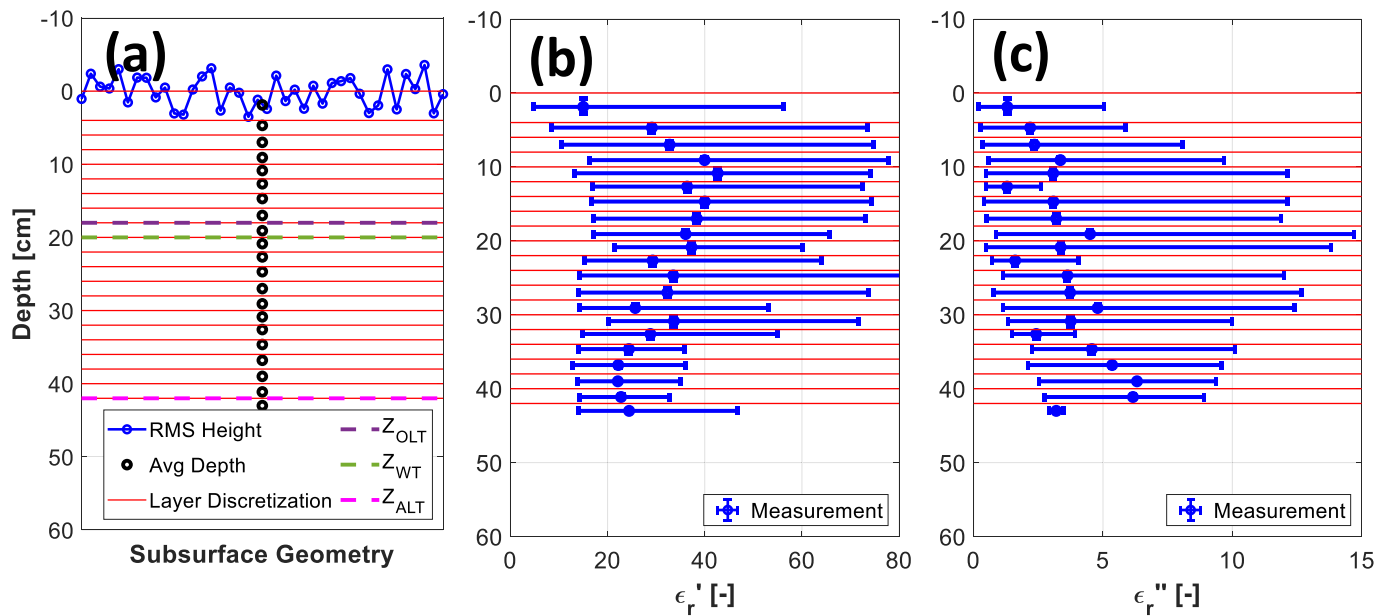


Fig. 11. (a) A schematic of the subsurface geometry, which consists of a discretized multi-layered dielectric structure along with surface roughness height behavior. The SPM accepts the dielectric profile at average depth points. (b-c) The in-situ range of real and imaginary parts of dielectric permittivity for all 8 sampling locations.

situ measurements. The laboratory soil samples were initially divided into organic and mineral categories (Fig. 6). The OM distribution of the mineral samples mainly varies between [0 – 20] % and based on the mineral texture analysis as shown in Table 2, the mineral soil can be roughly divided into coarse and fine texture classes. The coarse texture

class mainly includes sandy loam (FB-1, SGW-1), while the fine soil class is silty clay loam (SGW-2, HV-1, HV-2, ICC-1, ICC-2, IMN-1). The overall model performs better for finer soil textures (silty clay loam) for both real and imaginary parts of the dielectric. Although the samples with finer textures tend to contain higher OM content, the overall real part of

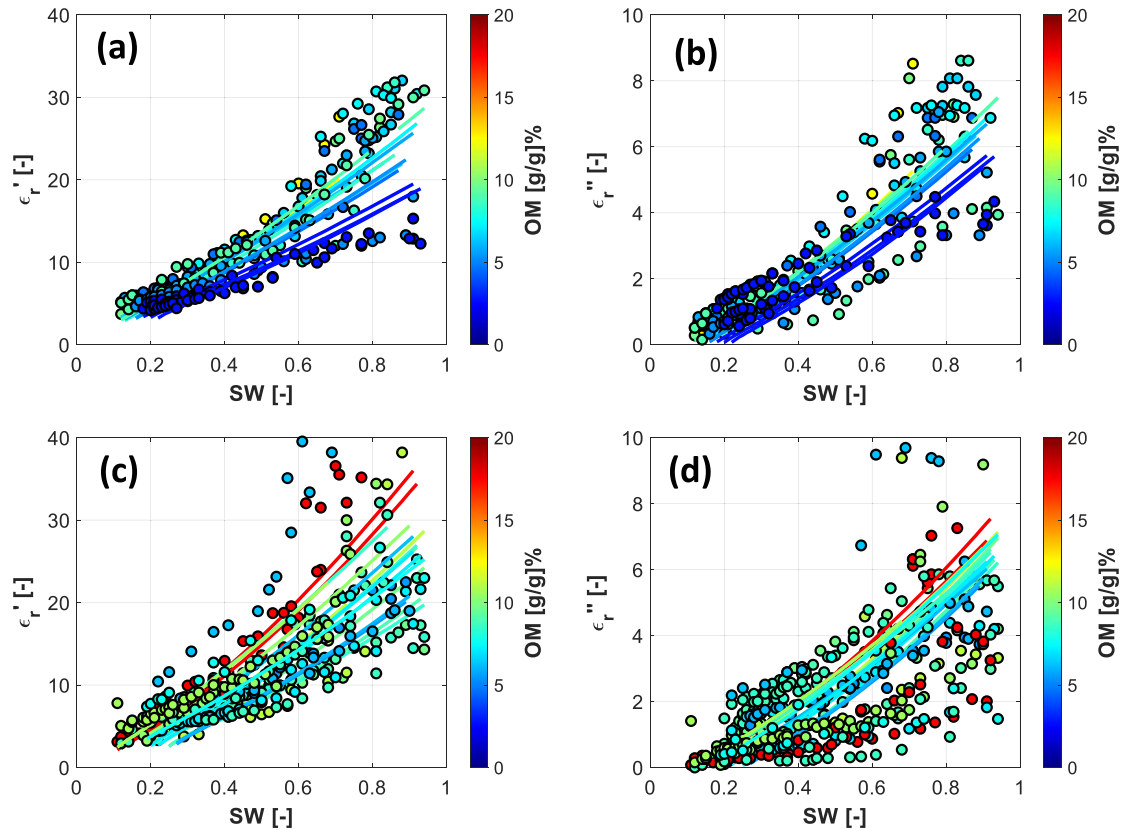


Fig. 12. Mineral soil dielectric behavior. In all cases the x-axis shows the soil saturation fraction, and the colour bar represents the OM content for each soil sample. (a) Real part of complex permittivity for sandy loam that includes FB-1 and SGW-1 samples. (b) Imaginary part of the complex permittivity for sandy loam soil. (c-d) Real and imaginary parts of the complex permittivity for silty clay loam that includes the SGW-2, HV-1, HV-2, ICC-1, ICC-2, and IMN-1 sites.

the dielectric permittivity exhibits smaller values compared with coarser textured samples at the same soil saturation level. Note that in Fig. 12, each colour corresponds to a single soil sample, in which the dielectric permittivity was measured two times for the full range of saturation.

For validating the organic samples, we divided them into two sub pools covering the respective OM ranges [60–80] % and [80–100] %. As stated in Table 2, the mineral texture for organic soil wasn't available, mainly due to the lack of sufficient mass to perform texture analysis. Therefore, for the model simulation, we used the average mineral texture of the deeper active layer sampled from each soil pit in the Alaskan North Slope. In the case of the Interior Alaska soil samples, a fraction of Sand = 36 % and Clay = 25 % was used to represent the typical mineral texture of all samples. The model behavior was consistent with measurements for both ranges of OM content, and the model predicted the real and imaginary parts of the permittivity very well (Fig. 13). It is important to note that, given the small variation in organic soil porosity between 60 and 100 % OM, overall, the dielectric variation in the organic soils is similar. However, it appears that for a higher range of OM (>70 %), the dielectric tends to increase at a lower rate, indicating less sensitivity, compared to the lower range of OM (<70 %). Discussion on model sensitivity to OM and SW are beyond the scope of this work and will be addressed in a forthcoming paper.

The model was simulated for over 1500 measurement points (in-lab) encompassing a broad range in soil saturation levels for all 66 soil samples. Accordingly, a 1:1 plot was generated to compare the model predictions and measurements for both real and imaginary parts of the dielectric permittivity. These results indicate favorable model performance without any observable bias (Fig. 14a-b). The root mean square error (RMSE) was calculated as follows:

$$RMSE^j = \sqrt{\frac{\sum_{i=1}^{N_i} (\epsilon_i - \epsilon_i^{MODEL})^2}{N_i}} \quad (26)$$

where N_i is the number of soil dielectric measurement points for j -th soil samples, which may vary from [10–34] given the experiment situation. The term ϵ_i refers to the ground truth dielectric measurement for the i -th soil moisture level, and ϵ_i^{MODEL} is the model output as described in Eq. (23b), once the corresponding soil properties ($OM^i, SW_i^j, S^i, C^i, T, freq$) are inserted. The RMSE values for the real and imaginary parts of the dielectric were calculated separately and then plotted, as OM varies among the soil samples (Fig. 14c). Each point in Fig. 14c refers to a single soil sample; among all samples, the average RMSE for the real part of the dielectric is 4.7, and 1.1 for the imaginary part (Fig. 14.d).

In this study, individual samples were not analyzed to compare their corresponding measurement and organic soil dielectric model behavior. Rather, we arranged the samples into mineral soil with fine and coarse texture, and organic soil categories with high [80–100], and low [60–80] concentration. The individual soil measurement and model behavior for both real and imaginary parts of the dielectric permittivity are shown in the supplement. Each fig. (S1 to S12) is associated with a sampling location listed in Table 2 and consists of multiple sub-figures corresponding to the identifiers listed in Table 2. As mentioned above, the number of (ϵ, SW) measurement pairs for each sample might be as large as 34, however in plotting the figs. (S1 to S12), we averaged the measurement points across the soil saturation range at intervals of 0.1 [–]. Therefore, plots are shown with error bars.

For each subplot, the soil identifier (ID), organic matter content, and corresponding RMSE for both real and imaginary parts of the dielectric are listed. The legacy mineral soil dielectric behavior (e.g., such as those

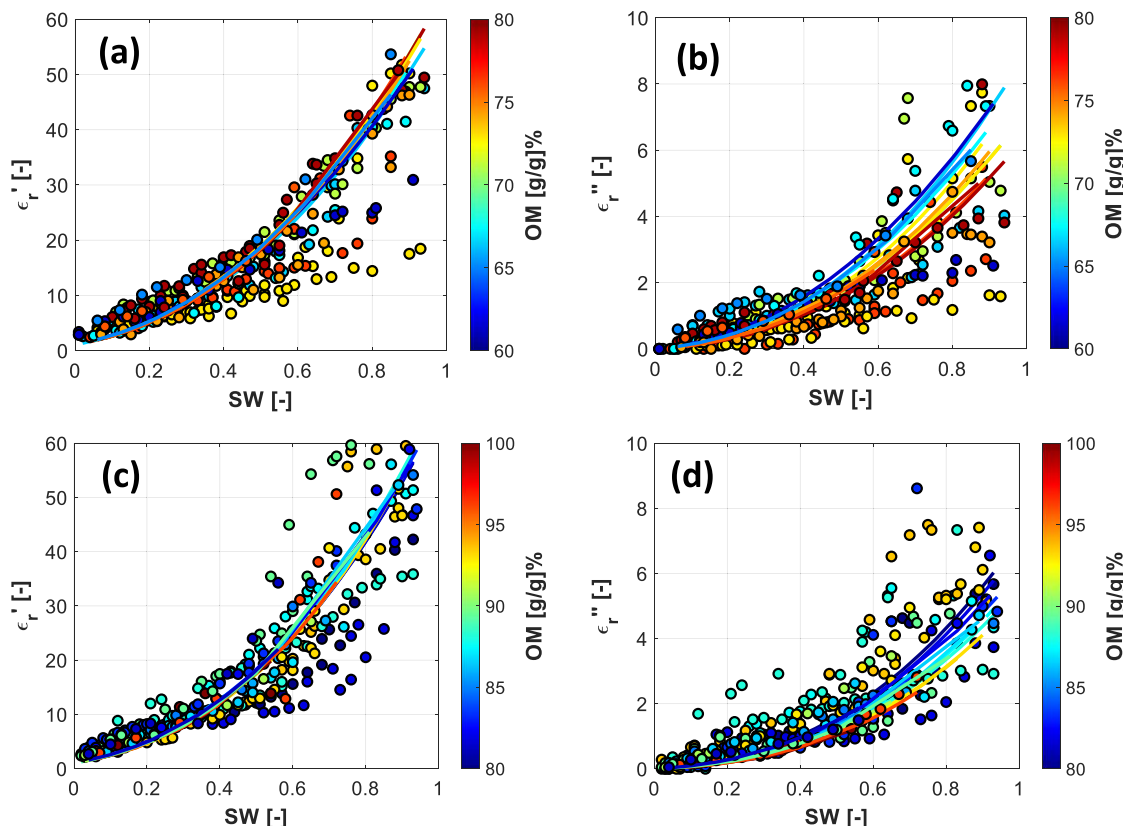


Fig. 13. Organic soil dielectric behavior. (a-b) Real and imaginary parts of the complex permittivity for the organic soil with OM variation between [60–80] %. (c-d) Real and imaginary parts of the complex permittivity for the organic soil with OM variation between [80–100] %.

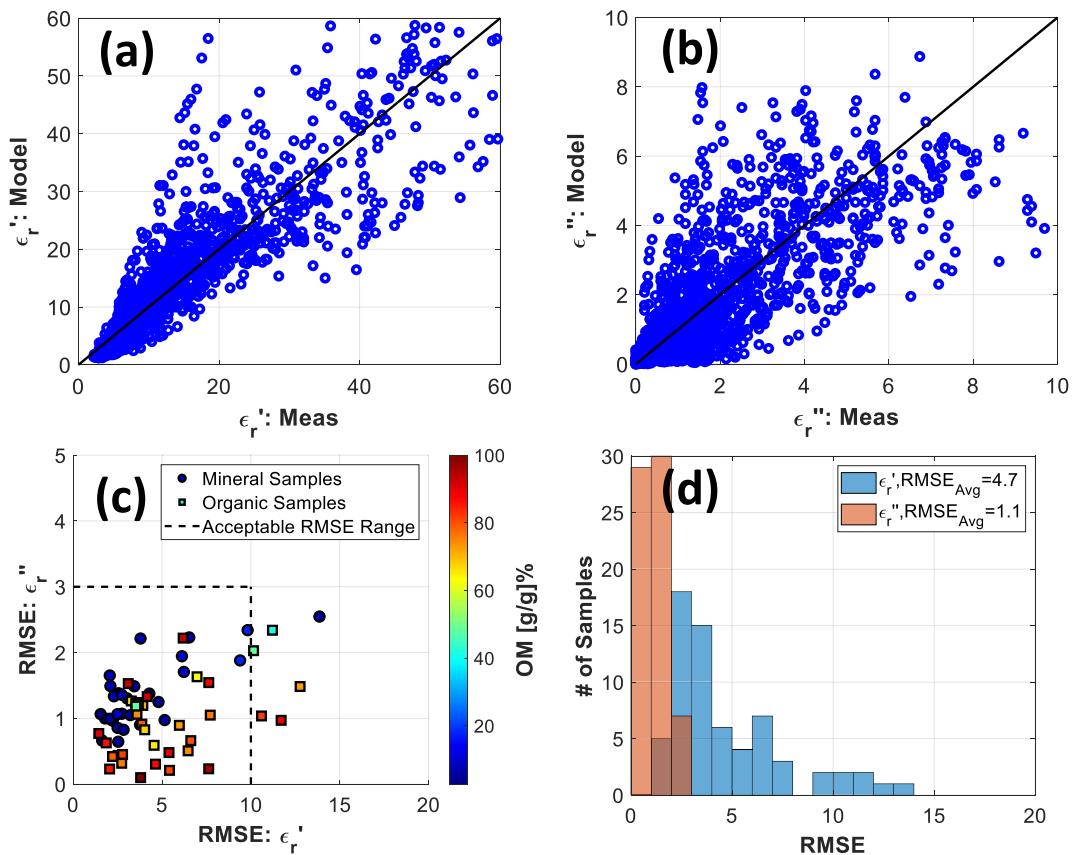


Fig. 14. (a) 1:1 plot of the real part of dielectric permittivity measurements against the model for all data points (dielectric for various soil moisture levels across all soil samples). (b) 1:1 plot for the imaginary part of the soil dielectric. (c) RMSE variation of the real and imaginary parts of soil dielectric properties of all soil samples, where each point represents a soil sample. (d) The histogram of RMSE for both real and imaginary parts of all soil dielectric properties.

reported in Hallikainen et al. (1985) show a curvature which is in agreement with our measurements; however, our model curve is slightly concave, which may reflect limitations of the model since a lower soil moisture simulation model cannot be used due to soil water retention curve limitations.

3.2. Organic soil dielectric model validation in field

In addition to the laboratory measurement-based validation, the model performance was also assessed against in-situ soil profile dielectric measurements collected during the 2018 field campaign. For this purpose, measurements from three soil pits (SGW-2, HV-1, and ICC-1) were selected for the model validation assessment out of eight total soil pits characterized over the Alaskan North Slope. The measured organic matter content and soil saturation profile were adapted from our previous work, and the profile model was fitted to the measurements using the Eq. (21a-c). As stated in Eq. (23b), the model inputs consist of the profiles of organic matter, soil saturation, temperature, and sand and clay fractions, where the total variation for all North Slope sampling locations is shown in Fig. 10. Model outputs for a representative selection of sites (SGW-2, HV-1, and ICC-1) are shown in Fig. 15 (Fig. 15a-b, 15e-f, 15i-j). Furthermore, a 15 % error was introduced to the model profile parameters to account for possible error contributed from field measurements. Note that in cases where the error simulation exceeds the physical valid range of OM or SW, the range was limited to stay below 100 % or 1, respectively.

The model and error simulations show acceptable agreement with the measurements for the real part of the dielectric permittivity through the active layer profile for all sites (Fig. 15c, g, and k). It appears the model can capture the fine variation of the soil dielectric profile, where a

smaller dielectric near the surface is associated with higher OM content and lower soil saturation fraction, and much lower variation in the deeper layer corresponds to the saturated homogeneous mineral layer. However, the model underestimates the imaginary part of the dielectric for all the sites except SGW-2; further elaboration on the underlying reasoning for this observation is provided in the discussion section.

4. Discussion

4.1. Empirical modeling an inevitable necessity

Existing literature on soil dielectric modeling (organic or mineral) is abundant with empirical models and over (or hyper) parametrization schemes used to minimize the RMSE and enhance the fit between model predictions with measurements. Some of the drawbacks of such empirical approaches are discussed in the introduction, including limited validity (due to limited samples) and potential unrealistic model behavior. Given the limited understanding of tundra soil processes and sparse availability of Arctic observational data, some empirical modeling is an inevitable necessity and can be effective as long as the models are developed from a large representative pool of soil samples and conditions, and the corresponding model predictions are physically realistic. Furthermore, the fundamental basis of this work is to produce a physics-based model for tundra that relates a set of soil physical properties to soil dielectric behavior. Further enhancements in model design and performance are anticipated as Arctic soil data and other complementary observations continue to be collected and analyzed.

Two parameters that include the overall water-in-soil electrical conductivity (σ_w), and the dielectric mixing model term (α) require an empirical approach for optimal performance. Given that a measure of

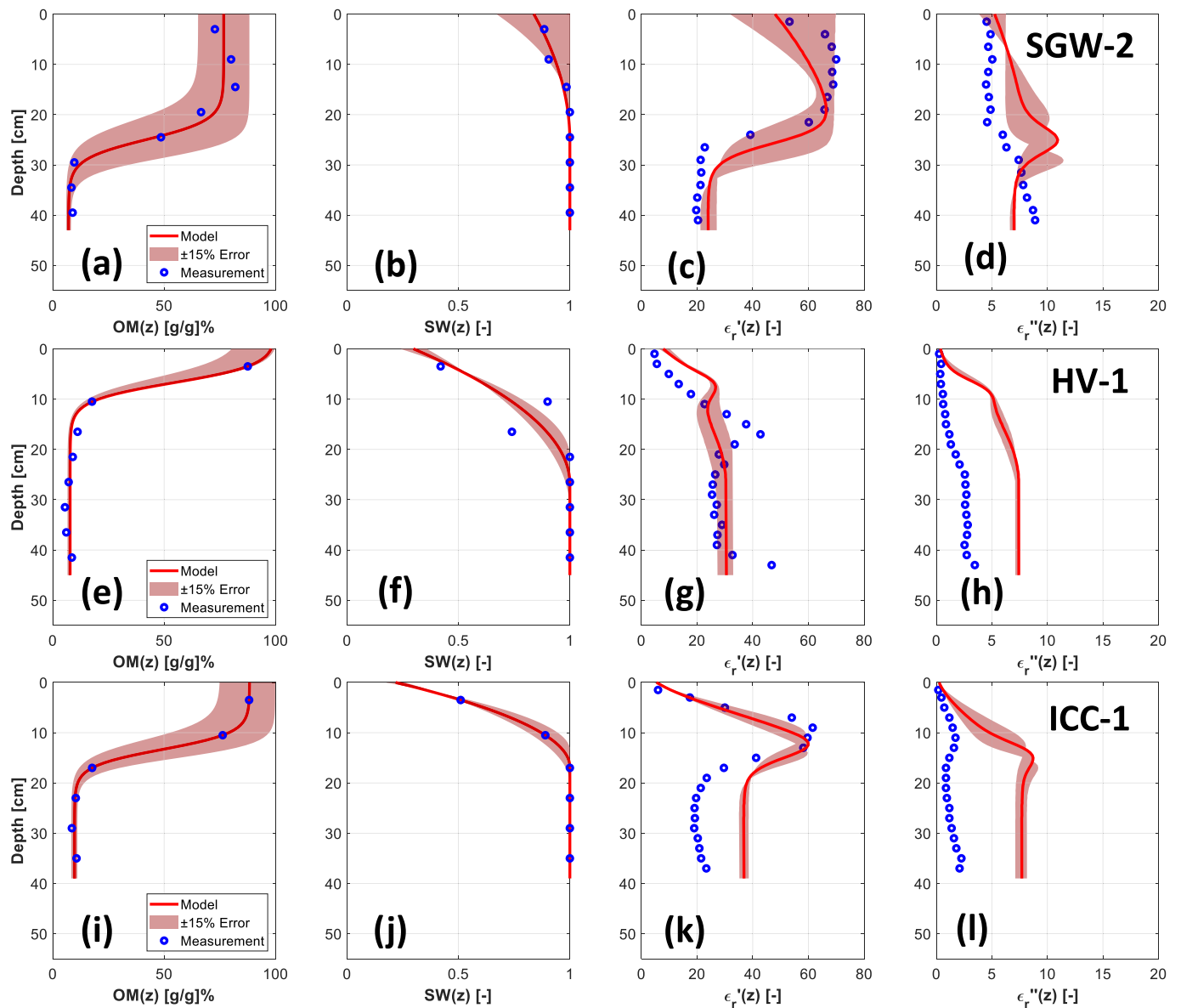


Fig. 15. Validation of the dielectric model against in-situ dielectric measurements. In all cases, measurements are shown with blue dots, the profile models are plotted with a red line, and the shaded red area represents the model as input profile parameters are perturbed to account for a 15 % error. The OM, SW, real, and imaginary part of dielectric for (a-d) SGW-2, (e-h) HV-1, and (i-l) ICC-1. (For interpretation of the references to colour in this figure legend, the reader is referred to the web version of this article.)

soil salinity wasn't available, the water-in-soil electrical conductivity was treated as an optimization variable to fit the imaginary part of the soil dielectric permittivity to the measurements.

A correlation analysis revealed that σ_w tends to increase with organic matter, sand and clay fractions, in accordance with the following relationship:

$$\sigma_w = 0.021 \times \tilde{f}_v^{OM} + 0.093 \times \tilde{f}_v^S + 0.294 \times \tilde{f}_v^C \quad (27a)$$

$$\alpha = 0.357 \times \tilde{f}_v^{OM} + 1.048 \times \tilde{f}_v^S + 0.987 \times \tilde{f}_v^{Si} \quad (27b)$$

where \tilde{f}_v^{OM} is the normalized volumetric fraction of total organic matter ($\tilde{f}_v^{OM} = \tilde{f}_v^{SOM} + \tilde{f}_v^{RB}$), and \tilde{f}_v^S , \tilde{f}_v^C , \tilde{f}_v^{Si} are normalized volumetric fractions for sand, clay, and silt. Subsequently, further analysis revealed a high correlation between $(\tilde{f}_v^{OM}, \tilde{f}_v^S, \tilde{f}_v^{Si})$ and the dielectric mixing model term (α) as described in Eq. (27b).

The optimized values (designated as measurements) along with the models for all soil samples and the simulation for a specific mineral texture of S = 36 %, and C = 25 % for the whole range of OM was then analyzed and showed general agreement between model and optimized values (Fig. 17). The optimized values (σ_w, α) for each soil sample were initially found based on a simulated annealing (SA) optimization scheme, where SA gave the best fit in minimizing the RMSE between the measured and estimated dielectric from Eq. 26. Accordingly, we refer to (σ_w, α) driven from SA as the measurement. The empirical model suggested in Eq. 27 was then found based on the correlation study of σ_w and α with soil properties.

Overall, a higher water-in-soil electrical conductivity is observed for mineral soil compared to more organic soil, which can be attributed to higher cation exchange capacity for mineral soil compared to organic soil (Fig. 16.a). As shown in the Results section, the model performs well in predicting the real and imaginary parts of dielectric permittivity for all lab samples (Figs. 12 and 13). However, the model validation against

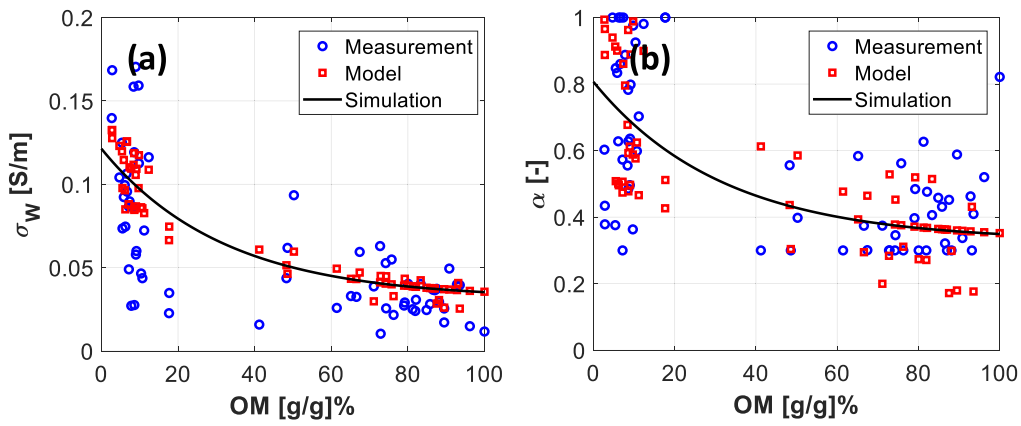


Fig. 16. Empirical modeling minimized the RMSE of the dielectric model against measurements over the range of OM conditions. In each plot, the blue dots represent the values that were found based on simulated annealing to minimize the RMSE of the soil dielectric model. The red squares show the model predictions derived from Eq. (24), and the black line plots the model simulations for an average soil containing 36 % Sand and 25 % Clay. (a) Soil water electrical conductivity (σ_w), behavior and (b) the mixing model term (α). (For interpretation of the references to colour in this figure legend, the reader is referred to the web version of this article.)

the in-situ dielectric profile model failed to capture the imaginary part, where the main contributor to the discrepancy between the model and in-situ observations is field measurement error. Particularly, the TERO 12 probe measurement is more susceptible to error in field deployments due to improper connections between probe needles and surrounding soil (TEROS 12 manual). Therefore, in an ideal measurement procedure, such as the controlled environment in the lab, where the probe is inserted within the soil layer, the measurement is more reliable. The redundancy of the measurement in the lab also further supports this observation.

The dielectric mixing model term (α) also monotonically decreases as OM increases, and the values vary between [1–0.3] for better fitting of the model to measurements. For values equal to 0.5, the dielectric

mixing model turns into a refractive index mixing model, and for pure mineral soil, it has been shown that a value of around 0.65 provides the best fit (Peplinski et al., 1995). Furthermore, as mineral texture becomes coarser, the values for α tend to be around 1 (not shown), while the optimized values of α for the organic soil are in the lower range of around 0.4.

4.2. Frequency and temperature behavior of soil dielectric model

The model validation results were obtained using dielectric measurements from the TERO 12 dielectric probe, which operates at 70 MHz. However, the radar instruments flown during the ABoVE Airborne Campaign in Alaska operate at higher frequency ranges (P- and L-

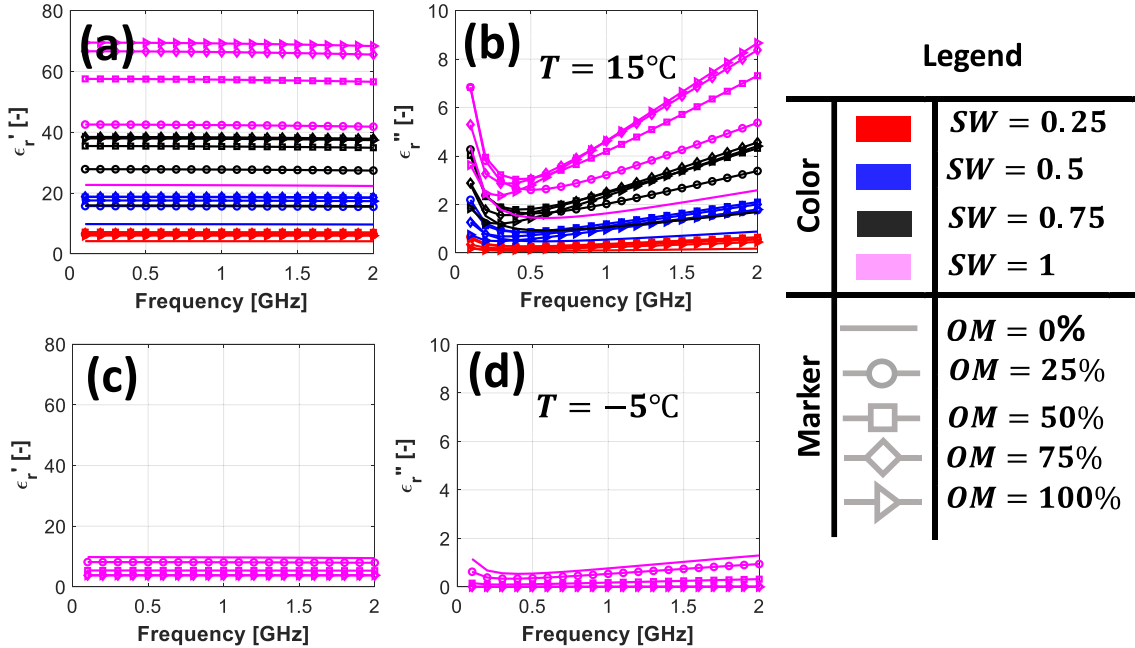


Fig. 17. The frequency behavior of the developed soil dielectric model under thawed and frozen conditions. The colour legend represents the soil saturation ranges (red shows the 0.25 saturation fraction, blue for 0.5, black for 0.75, and magenta shows fully saturated soil behavior). The markers represent the organic matter contents, where the unmarked plot shows 0 % OM content (pure mineral soil), and respectively the circle, square, diamond, and triangle symbols correspond to [25 %, 50 %, 75 %, and 100 %] OM contents. (a-b) The model simulation for above zero temperatures represents the real and imaginary parts of the dielectric behavior as frequency, OM content, and saturation fraction vary. (c-d) Shows the model simulation for saturated soil with variable frequency and OM at sub-zero temperatures. (For interpretation of the references to colour in this figure legend, the reader is referred to the web version of this article.)

bands). Therefore, studying the behavior of the soil dielectric model over these frequencies is of interest (Fig. 17). The soil dielectric model was simulated for the frequency range between [70 MHz – 2000 MHz] for multiple saturation points and a representative class of organic soil. The model simulation was conducted at sub-zero ($T = -5^\circ\text{C}$) and above-zero ($T = 15^\circ\text{C}$) temperatures, as representative values for freeze and thawed state. The frequency response of the soil dielectric was flat for the real part with negligible changes, whereas the imaginary parts exhibited more variation within the range, particularly for more saturated soil (Fig. 17a-b). This observation is consistent with the previous measurement for the mineral soil counterpart and mainly corresponds to the frequency response of the water dielectric behavior (Dobson et al., 1985; Hallikainen et al., 1985; Ulaby et al., 2014). Note that the model simulation for subzero temperatures was only conducted for saturated soil consistent with the model design (Fig. 17c-d).

The dielectric measurement provided in this work was conducted at room temperature ($\sim 22^\circ\text{C}$). However, given the complex temperature variation in Arctic soil, the model incorporates temperature as a dynamic input by modeling the freeze/thaw state. Therefore, the dielectric behavior of organic soil is studied as temperature varies from subzero (frozen) to above zero (thawed) conditions. Given the limitation in freeze/thaw modeling, the simulation is conducted for saturated soil, and only for P-band at 435 MHz.

4.3. Comparison between the behavior of existing organic soil dielectric model

As discussed in the introduction, the major difference between the model developed in this work and the existing organic soil dielectric models (see Fig. 1) is the treatment of water subphases. Previous works divided water into discrete phases, including bound, transient, and free water. In contrast, our work considered a continuous phase for water, where the associated dielectric properties were fully characterized using water matric potential, the Eyring equation, and the Debye model. A fair comparison between the performance of our model against other prevailing organic soil dielectric models can be performed from multiple perspectives: 1) parametrization, 2) model simulated behavior, and 3) validation at 70 MHz.

4.3.1. Parametrization and bound water argument

We first focused on model parametrization, and particularly addressed how the bound water fraction, soil bulk density, and wilting point were characterized in previous work. For the comparison, we implemented the Park et al. (2019, 2021), Mironov et al. (2019), and Savin et al. (2022) methods using spectroscopic and single frequencies (1400 and 435 MHz), respectively.

While the work presented here does not address bound water as a sub-component, we use the assumption that considers the maximum bound water fraction equal to the soil moisture at wilting point (Bakian-Dogaheh et al., 2022d). Accordingly, Park et al. (2019, 2021) used the parameterization provided by Jin et al. (2017), Yang et al. (2014), whereas Mironov et al. (2019) developed the model based on curve fitting and used Hossain et al. (2015) to account for OM variation. Similarly, Savin et al. (2022) found the bound water fraction based on curve fitting. For the purpose of model simulation, we assumed that the first transition points suggested in Mironov, and Savin's works are virtually identical to the wilting point. In all model simulations the temperature was assumed to be 20°C . Therefore, the behavior of the wilting point can be described as follows:

$$\theta_{wp}^{KBD} = \theta(\psi_m = -1500\text{kPa}) \quad (28a)$$

$$\theta_{wp}^{Park-2019} = 0.02982 + 0.089 \times C + 0.00786 \times OM \quad (28b)$$

$$\theta_{wp}^{Park-2021} = 0.02982 + 0.089 \times C + 0.0065 \times OM \quad (28c)$$

$$\theta_{wp}^{Savin} = 63 \times 10^{-3} + 4.23 \times 10^{-4} \times OM - 1.84 \times 10^{-4} \times T - 4.65 \times 10^{-6} \times T \times OM \quad (28d)$$

$$\theta_{wp}^{Mironov} = (0.118 + 8.694 \times 10^{-4} \times OM - 10^{-4} \times T)(0.071 + 1.32 \times e^{-0.0412 \times OM}) \quad (28e)$$

where in this study wilting point is defined as the soil moisture at a matric potential of (-1500kPa). Park et al. (2019) accept clay and OM as inputs, and Savin et al. (2020) and Mironov (2019) require temperature and OM as inputs. We further compared the bulk density and porosity parametrizations in the existing models. As shown in Fig. 19, the model behavior for Park et al. (2019) exhibits a non-physical behavior for the range of OM beyond 35 %, (Fig. 18a, c). Furthermore, the wilting point in Park et al. (2019) tends to monotonically increase as OM increases, which is also inconsistent with observations and previous works such as (Kolka et al., 2011, Yi. et al., 2022). This finding further contradicts the argument that a higher OM content tends to contain a higher bound water fraction if we assume the wilting point as a proxy of bound water fraction.

The comparison of bound water between Savin et al. (2022) and Mironov et al. (2019) are not consistent. Another observation shows the consistency between bound water behavior of our work and Mironov et al., 2019. This is mainly due to the similar bulk density behavior between the two models. It is important to note that not all parameters were available for comparison; for instance, Savin and Mironov avoid using porosity in their parameterization.

The relationship between the presence of organic matter and bound water fraction (f_v^{BW}) in soil has been discussed in previous studies (Park et al., 2021). A major observation case relevant to the current study is the contrasting behavior in dielectric permittivity between mineral soil (ϵ_M) and organic soil (ϵ_O) at the same soil moisture level (θ), where the ϵ_M tends to be larger than ϵ_O (Fig. 20, model simulation). Park et al. (2021) indicated that this contrasting behavior is due to the larger amount of bound water in organic soil compared to mineral soil (Fig. 20). This claim ($\theta : \epsilon_M > \epsilon_O \rightarrow f_{v,M}^{BW} < f_{v,O}^{BW}$) can be discussed from two perspectives, initially from the comparison of soil moisture level (θ) and saturation level ($SW = \theta/\phi$), because of the porosity (ϕ) differences between the two soil types it is important to perform the comparison at the same saturation level rather than at a consistent soil moisture level. For the same saturation level, the ϵ_O tends to be larger than ϵ_M , which can be explained by a smaller bound water (equivalent to larger free water) fraction in organic soil compared to mineral soil ($SW : \epsilon_M < \epsilon_O \rightarrow f_{v,M}^{FW} < f_{v,O}^{FW}$).

As mentioned, a general misconception regarding organic soil is that a higher OM level corresponds with more soil particle surface area and therefore a larger bound water component ($\theta_{wp}^O > \theta_{wp}^M \Rightarrow f_{v,O}^{BW} > f_{v,M}^{BW}$). Such correspondence has led to false assumptions that presence of organic matter in soil manifest similar hydraulic behavior to the presence of clay particles soil, since clay particles also have relatively larger surface area and in turn larger bound water (wilting point). While the behavior over the lower range of OM is yet to be determined, for highly organic soil ($OM > 35\%$) such as peat, the larger OM fiber content (such as in Fibric or Hemic soils, also referred to as acrotelm) coincides with larger hydraulic conductivity and a smaller particle surface area, which results in a lower bound water content (wilting point). Thus, the hydraulic behavior of a highly fibrous peat soil can be more similar to sand than a clay mineral soil. Smaller OM fiber contents characteristic of Sapric (catotelm) soils are more decomposed and exhibit relatively lower hydraulic conductivity, larger surface area, and a larger bound water fraction.

In this study, we used root biomass (RB) measurements as a proxy for

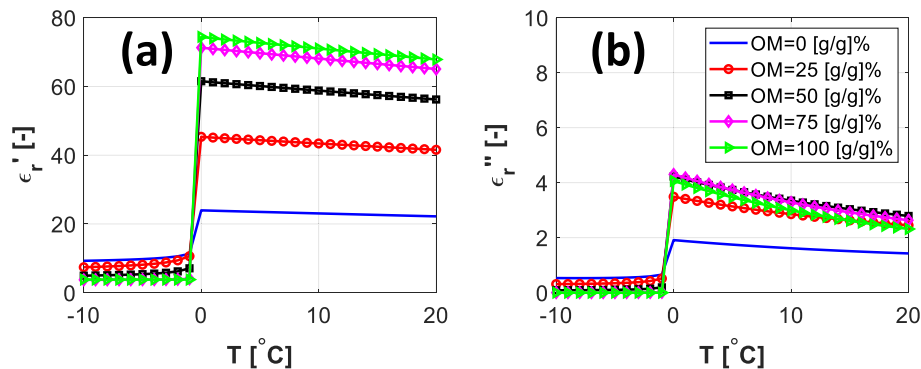


Fig. 18. The temperature behavior of the developed soil dielectric model at P-band for saturated soil. The colour legend represents the different OM levels represented (blue shows 0 %, red circle for 25 %, black square for 50, magenta diamond for 75 %, and green triangle shows fully organic soil behavior). (a-b) The model simulation shows the real and imaginary parts of the soil dielectric behavior as temperature and OM content vary. (For interpretation of the references to colour in this figure legend, the reader is referred to the web version of this article.)

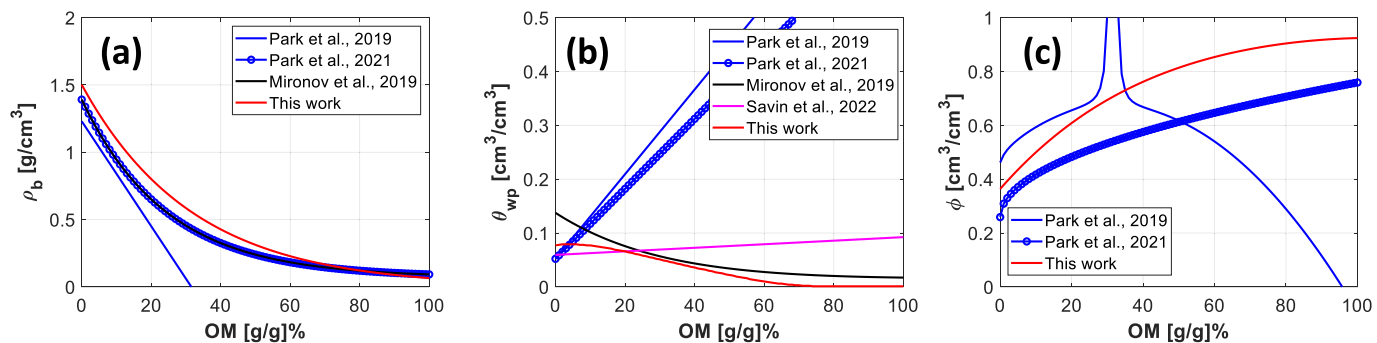


Fig. 19. Comparison of parameterization schemes used in prevailing organic soil dielectric models. In all figures, the blue lines show model results from Park et al. (2019) and the blue circles show results from Park et al. (2021); the black lines represent Mironov et al. (2019); Magenta lines correspond to Savin et al. (2022), and red lines show our work. (a) Shows the variation of bulk density used in previous work, where the Park et al. (2019) model exhibits non-physical values (negative or large bulk density) for larger OM. (b) Shows the behavior of the maximum bound water fraction, which was determined from the wilting point. (c) shows the porosity behavior of the above models. (For interpretation of the references to colour in this figure legend, the reader is referred to the web version of this article.)

fiber content. The introduction of RB and its soil organic matter (SOM) differentiation in our parameterization had a major impact on the model organic soil hydrology and dielectric behavior. The resulting model approach enables the development of soil dielectric curves for diverse Arctic soils with substantial variability in soil physical properties and across different spatial and vertical extents.

4.3.2. P- and L-band model behavior comparison

Another approach for comparing our model with other existing organic soil dielectric models is to compare the real and imaginary behavior of the models at 1400 MHz and 435 MHz for a constant temperature ($T = 20^\circ\text{C}$) over the full range of OM and soil moisture conditions. The major goal here is to further study the model performance and validity for potential use in physics-based radar retrievals. A comparison between our work and Park et al. (2019) shows that the models perform similarly for lower OM content (0 and 25 %). However, the Park et al. (2019) model parametrization is not valid at higher OM ranges, and the subsequent discrepancy between the two models increases drastically. The real part of the permittivity from Savin et al. (2022), which was developed at 435 MHz, performs similarly to Mironov et al. (2019), which works at 1400 MHz. However, the imaginary part of the dielectric behavior is not consistent as soil moisture increases. Furthermore, both models show minimal sensitivity to the organic matter content. This observation further emphasizes the importance of measurement methods. Both Mironov and Savin's models are based on a destructive measurement method that ground the soil samples (Fig. 21). The homogenized ground samples exhibits similar characteristics regardless of texture. Similar observations from mineral-only soils are

also applicable. In general, the Mironov models were developed using similar destructive grinding methods for mineral soil as well. Therefore, the coarser texture that includes a larger sand fraction after grinding performs similarly to clay (finer) soil (Mironov et al., 2010).

4.3.3. Validation of all models

A fair assessment and validation of all existing models against our entire validation pool (complex dielectric permittivity at 70 MHz), is challenging. Since either the available models do not accept frequency as input, or those that of spectroscopic models do not accept OM as an input (Fig. 2). The frequency exerts the largest impact on the imaginary part of soil dielectric, whereas for the real part, the frequency behavior of soil tends to be less dispersive and flat. To that end, we ran the Park et al. (2019), Mironov et al. (2019), and Savin et al. (2022) models with the inputs driven from our validation pool (derived from laboratory measurements). For each model, the corresponding estimated permittivity is compared with our measurements, and the RMSE was calculated according to Eq. (26). For the imaginary part of the soil dielectric, we translated the measured electrical conductivity to the corresponding frequency ($\epsilon_r'' = \frac{\sigma}{2\pi\epsilon_0 f_0}$) of each model.

Without considering the existing model validity range (Table 1), the RMSE analysis for the real part of the dielectric permittivity shows that our model performs better than the other models. The RMSE analysis for the imaginary part of the soil dielectric was performed at multiple frequencies and shows that the proposed model produces better estimates of the imaginary part of the soil dielectric at 70 MHz, 435 MHz, and 1400 MHz frequencies than the other models (Table 3).

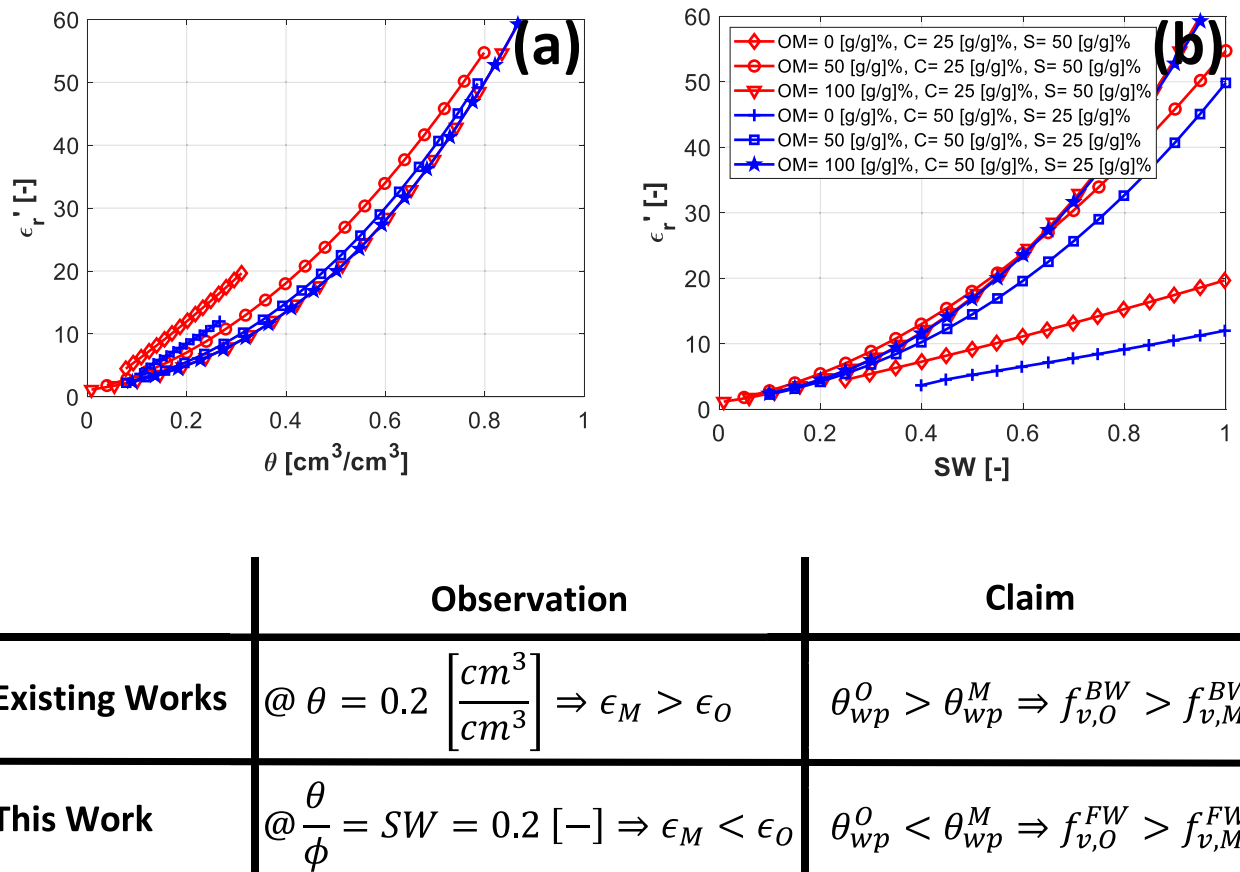


Fig. 20. Bound water argument. (a) Comparison of the real part of soil dielectric for organic and mineral soils at the same soil moisture level. High sand and clay fractions are simulated with corresponding red and blue curves. (b) Comparison for the same soil saturation level. Table shows the observations and claims about bound water from this study and other existing works reported in the literature. (For interpretation of the references to colour in this figure legend, the reader is referred to the web version of this article.)

4.4. Limitation of organic soil dielectric model

While the model introduced in this study incorporates a comprehensive measurement and modeling approach and demonstrates higher accuracy for dielectric mixture modeling of tundra soils than the other prevailing models, there are still limitations associated with this model that need to be discussed. This work initially focused on highly organic soils common in Arctic tundra, which exhibit certain features such as higher surface OM and lower moisture content than the deeper mineral soil of the active layer. The model parametrization developed in this work was based on soil matric potential measurement using the TEROS 21 porous disk probe, where the resulting matric potential measurement at lower soil moisture was more erroneous. Therefore, the resulting model has limitation in the lower soil moisture regime, and particularly for mineral soils. Future work needs more extensive measurement of soil water matric potential at lower soil moisture levels for less organic soil.

The lower range of soil moisture is limited to a water matric potential (ψ_m^{lim}) equivalent to $-100,000$ [kPa]. The inverse presence of soil moisture in Eq. (8) does not result in an unrealistic estimate, but what limits the lower end of the soil moisture (saturation) estimate is the asymptotic behavior of the soil water retention curve at the lower soil moisture range. Therefore, the organic soil dielectric model predictions at the lower saturation level (0.1) are not shown in Fig. 17. The empirical modeling and validation assessment in this work was conducted with this limitation. In a practical case such as physics-based remote sensing of Arctic soil, additional assumptions have to be made to simulate the lower saturation end for Mineral soil (e.g., for $\theta < \theta_{\psi_m^{lim}}$,

the $\psi_m = \psi_m^{lim}$), which can impose a small bias for mineral soil relative to the more accurate model predictions expected for highly organic soil (Fig. 22).

In Eq. (20) and for the measurement of soil water potential, the first three terms (ψ_p, ψ_g, ψ_o) were assumed negligible. While such assumptions might hold for the pressure potential (ψ_p) and gravitational potential (ψ_g), the osmotic potential (ψ_o) can be impacted by solute concentration, which in the case of Arctic soil primarily comprises of salt and dissolved organic matter. For salinity, the TEROS 21 manufacturer reports that an electrical conductivity larger than 10 dS/m can potentially result in erroneous matric potential readings by confounding the TEROS-21 capacitance measurement. However, the joint measurement of soil dielectric properties using TEROS-12 showed relatively small electrical conductivity in the range of < 1 dS/m for all soil samples, which results from very low salinity. Therefore, the osmotic potential due to salinity can be assumed negligible. On the other hand, the presence of dissolved organic matter, particularly for highly decomposed soil samples (with lower fiber content) can potentially impact the matric potential, since the Eq. (19) assumes the dielectric constant of the ceramic disk is not affected by other components and is only controlled by water within the ceramic disk. Other matric potential techniques, such as evaporation at relatively high soil pressure (e.g., HYPROP) and dew point for relatively low soil pressure (e.g., WP4C Dew Point Potentiometer), could be used in future work to capture more accurate water matric potential measurements. Nonetheless, the measurements provided from TEROS-21 do not change the generality of our approach in organic soil dielectric model development, and in characterizing

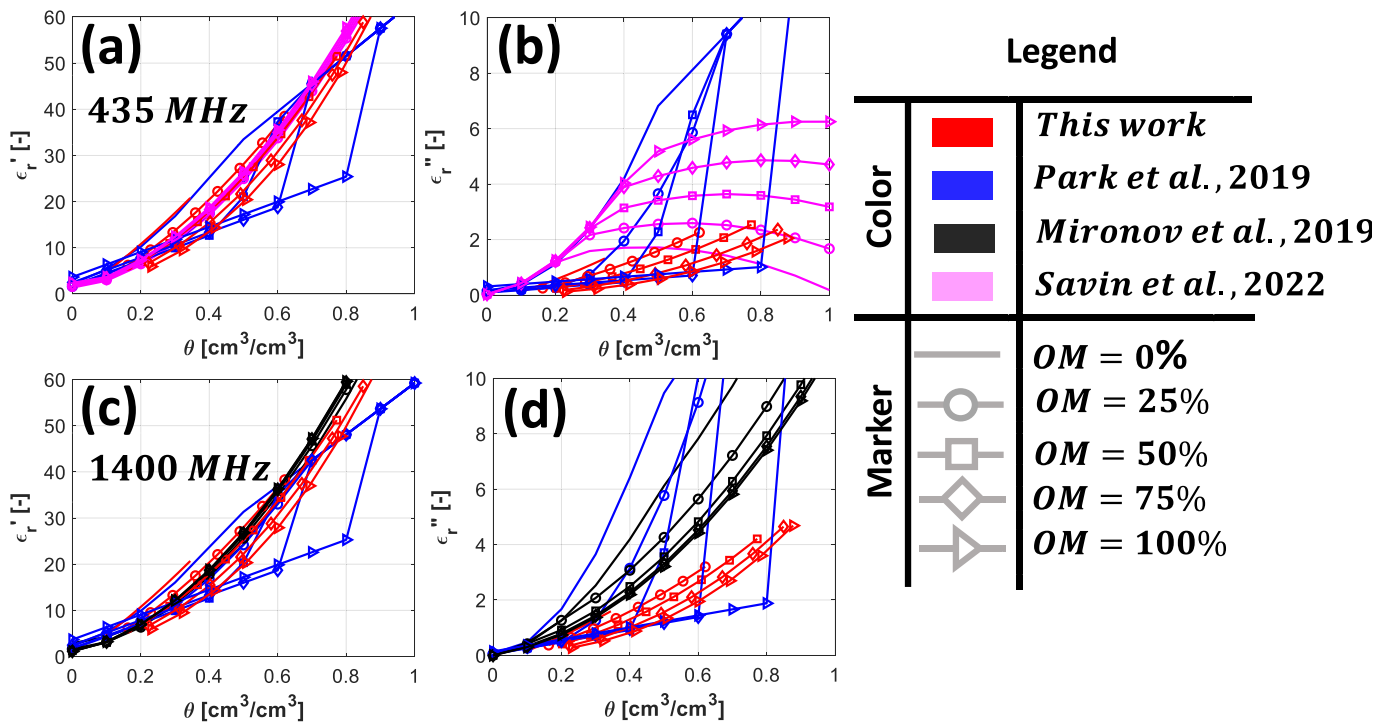


Fig. 21. Comparison of the existing organic soil dielectric models at 435 MHz, and 1400 MHz. The colour legend denotes the particular model, where the markers show the OM variation. (a) Model behavior at 435 MHz and (b) model behavior at 1400 MHz are presented.

Table 3

Model validation against the laboratory measurements for all 66 tundra soil samples.

RMSE with	ϵ'_r 70 MHz	ϵ''_r 70 MHz	ϵ'_r 435 MHz	ϵ''_r 1400 MHz
This work	4.7	1.1	0.4	1.2
Park et al., 2019	5.7	7.1	—	—
Savin et al., 2022	5.5	—	2	—
Mironov et al., 2019	5.6	—	—	2.7

water-in-soil dielectric properties from matric potential and estimated soil retention curves.

Additionally, the freeze-thaw modeling and the expansion behavior described in Section 2.1.2 is potentially much more sophisticated, particularly the freezing point of soil varies with dissolved solute concentrations, which should produce more gradual slopes near 0 [°C], and asymmetric behavior between freezing and thawing (e.g., see Devoie et al., 2022). Nevertheless, this model shows significant improvement in capturing the full soil moisture range in highly organic soils characteristic of the tundra permafrost active layer and is suitable for application to other Arctic soils.

4.5. Potential for retrieving water and carbon characteristics from radar observations

While the major focus of this study was to develop and validate a new organic soil dielectric model, the ultimate application of the model is integration within a physics-based radar retrieval framework to study the water and carbon characteristics of permafrost active layer soil using radar observation (section 2.4). Once the soil dielectric model is developed and validated, it can be used to study the feasibility of retrieval for a few locations. To this end, five sites from the Circumpolar Active Layer Network (CALM) were selected within the Deadhorse flight line from the ABoVE airborne campaign (Brown et al., 2000; Miller et al., 2019). For each location, the associated backscattered P-band data were acquired from the August 2017 flight, and accordingly, the forward solver was simulated to construct a data cube that consists of state parameter variations (Fig. 23a, Table 4). Additionally, we set the sand and clay fractions as 36 %, and 25 % respectively, OM profile parameters were set ($\beta = 0.5$, $OM_M = 7\%$) from soil inventory records, and the surface temperature was assumed to be $T_{z0} = 8^{\circ}\text{C}$. Notice that the temperature profile behavior is controlled by the z_{ALT} and T_{z0} according to Eq. (21c).

Once the state parameters data cube is constructed, the corre-

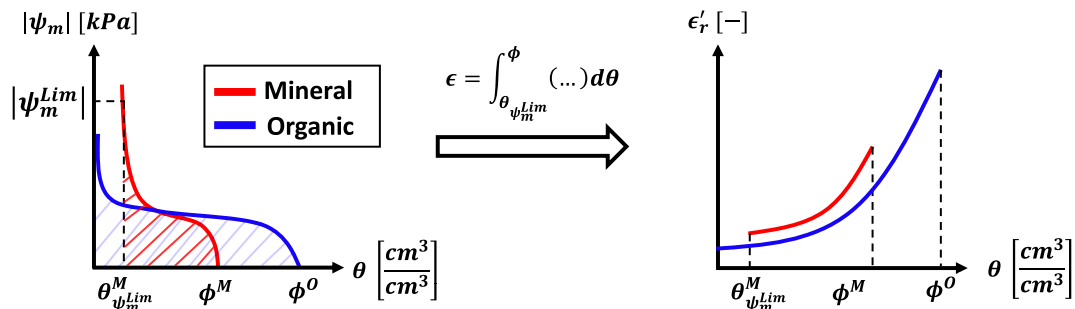


Fig. 22. The limitation of organic soil dielectric model.

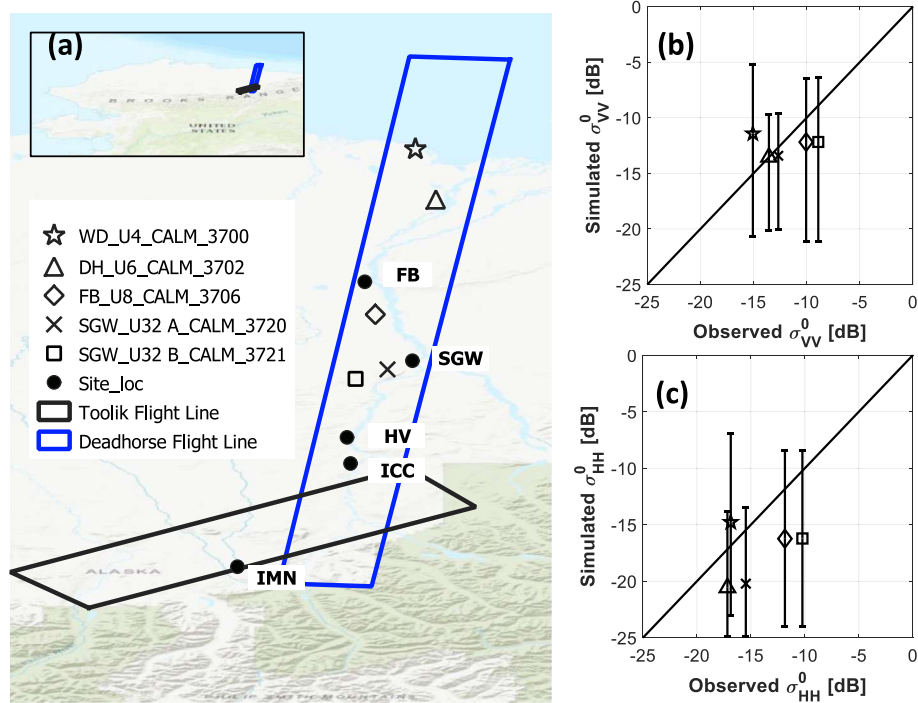


Fig. 23. The feasibility of retrieving permafrost active layer subsurface water and carbon characteristics using radar (P-band) observation. (a) Shows the CALM sites, our North Slope sampling locations (filled circles), and two ABoVE Airborne Campaign flight swaths. (b) shows the variation of the simulated backscattering coefficient for VV polarization, where the range of input parameters are adapted from Table 3, along with radar observation for each point. (c) Accordingly shows the variation of simulated backscattering coefficient for HH polarization.

Table 4

List of state parameters in the retrieval scheme, assumptions and sets of parameters that were fixed based on ancillary field data and the literature. For the unknown parameters and measurements, the range of variation is provided; in data cube development the unknowns are discretized with corresponding discretization steps.

Parameter Definition	Symbol	Status	Unit	Range/Value	Discretization
Surface Organic Matter	OM_{z0}	Unknown	[g/g] %	[10 – 100]	10
Organic Layer Thickness	z_{OLT}	Unknown	[cm]	[16 – 44]	4
Surface Saturation	SW_{z0}	Unknown	[– 1]%	[0.25 – 1]	0.25
Water Table Depth	z_{WT}	Unknown	[cm]	[16 – 44]	4
Soil Roughness RMS Height	h	Unknown	[cm]	[0.5 – 4]	0.5
Active Layer Thickness	z_{ALT}	Unknown	[cm]	[28 – 60]	4
OM Profile Shape Factor	β	Known	(1/m)	50	(–)
Mineral Layer Organic Matter	OM_M	Known	[g/g] %	7	(–)
Sand Fraction	S_{avg}	Known	[g/g] %	36	(–)
Clay Fraction	C_{avg}	Known	[g/g] %	25	(–)
Surface Temperature	T_{z0}	Known	[°C]	+ 8.0	(–)
Backscattering Coefficients	$\sigma_{HH}^0, \sigma_{VV}^0$	Measurement	[dB]	[– 35 – 0]	(–)
Incident Angle	θ_{inc}	Measurement	[degree]	[15 – 60]	(–)

sponding soil profile models ($OM(z)$, $SW(z)$, $S(z)$, $C(z)$, $T(z)$) for each realization are fed into the soil dielectric model to arrive at the soil dielectric profile behavior. Consequently, the layered dielectric structure adapted from MODEL output, roughness height, and incidence angles (θ_i) from P-band radar measurement was applied to the backscattering forward model known as SPM (The layered dielectric structure is depicted in Fig. 11, section 2.4). The variation of simulated backscattered coefficients for both HH and VV polarization is then compared to the 1:1 plot that shows the feasibility of retrieval of active layer soil subsurface water and carbon characteristics for each tundra subregion as it crosses the 1:1 line (Fig. 23b, c).

In Arctic tundra, and at a radar pixel level (e.g., ABoVE Airborne Campaign conventional data product $\sim 30 \times 30 \text{ m}^2$), the heterogeneity of OM and soil moisture both spatially and along the vertical profile can be substantial. We collected 66 soil samples at diverse locations and across different depths, which served as the foundation for validating the presented soil dielectric model. While a representative pool of

samples is important for validation purposes, the soil dielectric modeling as described in the general form in Eq. 23b is agnostic to radar pixel soil heterogeneity.

In the above case study for retrieving active layer subsurface water and carbon characteristics using radar observations, the organic soil dielectric model effectively links the surface and subsurface soil parameters (e.g., OM and soil saturation profile) to the equivalent soil dielectric profile, which can then be applied to a multi-layered electromagnetic scattering model to derive the corresponding radar backscatter coefficients (Fig. 11). A major assumption for retrieval purposes is to model the radar pixel as a multi-layered dielectric structure with dielectric properties controlled by soil OM, soil saturation, and other constituents as described in Eq. 23b. The other building blocks in a physics-based retrieval algorithm were described in subsection 2.3.1, where we briefly discussed the active layer soil profile model, and in section 2.4, which describes how equivalent soil dielectric profiles play a role in calculating the radar backscattering coefficients (e.g. see Fig. 8 in

Bakian-Dogaheh et al., 2022).

The influence of surface and sub-surface heterogeneity on physics-based radar retrievals of Arctic soil parameters and on estimates of water and carbon characteristics at local and regional scales requires further research.

5. Conclusion

This work provides a comprehensive organic soil dielectric characterization based on the largest-known sampling campaign to-date for Arctic permafrost active layer soils. A physics-based dielectric model that leverages the hydrological properties of soil was developed to predict the water-in-soil dielectric behavior. Subsequently, the water-in-soil dielectric properties were incorporated into a dielectric mixing model to arrive at effective soil dielectric properties. The model was validated against a large pool of soil samples, which covers the realistic range of organic matter and soil moisture conditions. The model inputs consist of basic soil physical properties, including soil saturation, organic and mineral texture, and additionally, accept temperature and frequency.

The major goal of the organic soil dielectric model is for integration with a physics-based radar retrieval algorithm for remote sensing applications to study the dynamics of water and carbon in organic-rich permafrost active layer soil. To this end, a feasibility study of radar retrieval was conducted, in which the results exhibit the possibility of retrieving subsurface profile parameters such as organic matter and soil saturation profile along with the active layer thickness.

Future work may include adding more representative soil samples for the range of OM between 20 and 60 %, which were lacking in the current study. A dedicated validation of the soil dielectric at lower frequencies, particularly P- and L-bands (Bakian-Dogaheh & Moghaddam 2022b) may also be employed to better inform ABoVE airborne SAR retrievals and planning for next generation P- and L-band satellite SAR missions such as European Space Agency (ESA) BIOMASS and NASA and ISRO Synthetic Aperture Radar (NISAR) missions (Rosen et al., 2017; Le Toan et al., 2011). Additionally, a more controlled thermal measurement experiment for subzero temperatures is needed to improve dielectric model response to variations in unfrozen water content during freeze/thaw transitions, which strongly influence soil OM decomposition and greenhouse gas emissions (Zona et al., 2016), ALT and permafrost stability (Park et al., 2016). Overall, the results of this study and the new physics-based soil dielectric model are expected to improve remote sensing based monitoring and physical process modeling of permafrost active layer soils, leading to better understanding of the changing Arctic and its role in reinforcing global climate change.

CRediT authorship contribution statement

Kazem Bakian-Dogaheh: Writing – review & editing, Writing – original draft, Validation, Project administration, Methodology, Investigation, Formal analysis, Data curation, Conceptualization. **Yuhuan Zhao:** Writing – review & editing, Investigation. **John S. Kimball:** Writing – review & editing, Funding acquisition. **Mahta Moghaddam:** Writing – review & editing, Supervision, Funding acquisition.

Declaration of competing interest

The authors declare that they have no known competing financial interests or personal relationships that could have appeared to influence the work reported in this paper.

Data availability

All data used in this manuscript are archived and available at the Oak Ridge National Laboratory Distributed Active Archive Center (ORNL DAAC): doi:3334/ORNLDaac/2149.

Acknowledgment

This work was supported by the NASA Earth and Space Science Fellowship (NESSF) Grant No. 80NSSC18K1410, and the Arctic Boreal Vulnerability Experiment (ABoVE) of the NASA Terrestrial Ecology program, under Grants NNX17AC65A (ABoVE Phase #1), 80NSSC19M0114 (ABoVE Phase #2), and 80NSSC22K1238 (ABoVE Phase #3).

Appendix A. Supplementary data

Supplementary data to this article can be found online at <https://doi.org/10.1016/j.rse.2024.114560>.

References

Akbar, R., Cosh, M.H., O'Neill, P.E., Entekhabi, D., Moghaddam, M., 2017. Combined radar–radiometer surface soil moisture and roughness estimation. *IEEE Trans. Geosci. Remote Sens.* 55 (7), 4098–4110 doi:1109/TGRS.2017.2688403.

Bakian-Dogaheh, K., Moghaddam, M., 2022. A new microwave imaging system for dielectric characterization of highly organic Arctic permafrost soil. In: 2022 IEEE APS/URSI IEEE, pp. 527–528 doi:1109/AP-S/USNC-URSI47032.2022.9886772.

Bakian-Dogaheh, K., Chen, R.H., Moghaddam, M., Yi, Y., Tabatabaeenejad, A., 2020. Above: active layer soil characterization of permafrost sites, northern Alaska, 2018. ORNL DAAC. doi:3334/ORNLDaac/1759.

Bakian-Dogaheh, K., Chen, R.H., Yi, Y., Kimball, J.S., Moghaddam, M., Tabatabaeenejad, A., 2022. A model to characterize soil moisture and organic matter profiles in the permafrost active layer in support of radar remote sensing in Alaskan Arctic tundra. *Environ. Res. Lett.* 17 (2), 025011 doi:1088/1748-9326/ac4e37.

Bakian-Dogaheh, K., Chen, R.H., Yi, Y., Sullivan, T.D., Michaelides, R.J., Parsekian, A.D., Schaefer, K., Tabatabaeenejad, A., Kimball, J., Moghaddam, M., 2023. Soil matric potential, dielectric, and physical properties, Arctic Alaska, 2018. ORNL DAAC. doi: 3334/ORNLDaac/2149.

Bircher, S., Andreassen, M., Vuollet, J., Vehviläinen, J., Rautiainen, K., Jonard, F., Kerr, Y.H., 2016a. Soil moisture sensor calibration for organic soil surface layers. *Geosci. Instrum. Methods. Data Syst.* 5 (1), 109–125 doi:5194/gi-5-109-2016.

Bircher, S., Demontoux, F., Razafindratisima, S., Zakhrova, E., Drusch, M., Wigneron, J.P., Kerr, Y.H., 2016b. L-band relative permittivity of organic soil surface layers—a new dataset of resonant cavity measurements and model evaluation. *Remote Sens.* 8 (12), 1024 doi:3390/rs8121024.

Blonquist Jr., J.M., Jones, S.B., Lebron, I., Robinson, D.A., 2006. Microstructural and phase configurational effects determining water content: dielectric relationships of aggregated porous media. *Water Resour. Res.* 42 (5) doi:1029/2005WR004418.

Boyarskii, D.A., Tikhonov, V.V., Komarova, N.Y., 2002. Model of dielectric constant of bound water in soil for applications of microwave remote sensing. *Prog. Electromagn. Res.* 35, 251–269 doi:10.2528/PIER01042403.

Brown, J., Hinkel, K.M., Nelson, F.E., 2000. The circumpolar active layer monitoring (CALM) program: research designs and initial results. *Polar Geogr.* 24 (3), 166–258 doi:1080/10889370009377698.

Buchner, R., Barthel, J., Stauber, J., 1999. The dielectric relaxation of water between 0 C and 35 C. *Chem. Phys. Lett.* 306 (1-2), 57–63 doi:1016/S0009-2614(99)00455-8.

Campbell, G.S., 1974. A simple method for determining unsaturated conductivity from moisture retention data. *Soil Sci.* 117 (6), 311–314.

Chapin, E., Chau, A., Chen, J., Heavey, B., Hensley, S., Lou, Y., Moghaddam, M., 2012. May. AirMOSS: An airborne P-band SAR to measure root-zone soil moisture. In: 2012 IEEE Radar Conference. IEEE, pp. 0693–0698 doi:1109/RADAR.2012.6212227.

CLM 5 documentation. n.d. (available at: <http://www.cesm.ucar.edu/models/cesm2/land/CLM50.Tech Note.pdf>).

Cosenza, P., Tabbagh, A., 2004. Electromagnetic determination of clay water content: role of the microporosity. *Appl. Clay Sci.* 26 (1–4), 21–36 doi:1016/j.clay.2003.09.011.

Devoie, É.G., Gruber, S., McKenzie, J.M., 2022. A repository of measured soil freezing characteristic curves: 1921 to 2021. *Earth Syst. Sci. Data* 14 (7), 3365–3377 doi: 5194/essd-14-3365-2022.

Dobson, M.C., Ulaby, F.T., Hallikainen, M.T., El-Rayes, M.A., 1985. Microwave dielectric behavior of wet soil-part II: dielectric mixing models. *IEEE Trans. Geosci. Remote Sens.* 1, 35–46 doi:1109/TGRS.1985.289498.

Dyck, M., Miyamoto, T., Iwata, Y., Kameyama, K., 2019. Bound water, phase configuration, and dielectric damping effects on TDR-measured apparent permittivity. *Vadose Zone J.* 18 (1), 1–14 doi:2136/vzj2019.03.0027.

Friedman, S.P., 1998. A saturation degree-dependent composite spheres model for describing the effective dielectric constant of unsaturated porous media. *Water Resour. Res.* 34 (11), 2949–2961 doi:1029/98WR01923.

Fuchs, M., Campbell, G.S., Papendick, R.I., 1978. An analysis of sensible and latent heat flow in a partially frozen unsaturated soil. *Soil Sci. Soc. Am. J.* 42 (3), 379–385 doi: 2136/sssaj1978.03615995004200030001x.

Gnatowski, T., Szatylowicz, J., Pawłuszkiewicz, B., Oleszczuk, R., Janicka, M., Papierowska, E., Szejba, D., 2018. Field calibration of TDR to assess the soil moisture of drained peatland surface layers. *Water* 10 (12), 1842 doi:3390/w10121842.

Hallikainen, M.T., Ulaby, F.T., Dobson, M.C., El-Rayes, M.A., Wu, L.K., 1985. Microwave dielectric behavior of wet soil-part 1: empirical models and experimental

observations. *IEEE Trans. Geosci. Remote Sens.* 1, 25–34 doi:1109/TGRS.1985.289497.

Hilhorst, M.A., Dirksen, C., Kampers, F.W.H., Feddes, R.A., 2001. Dielectric relaxation of bound water versus soil matric pressure. *Soil Sci. Soc. Am. J.* 65 (2), 311–314 doi: 2136/sssaj2001.652311x.

Hinzman, L.D., Kane, D.L., Gieck, R.E., Everett, K.R., 1991. Hydrologic and thermal properties of the active layer in the Alaskan Arctic. *Cold Reg. Sci. Technol.* 19 (2), 95–110 doi:1016/0165-232X(91)90001-W.

Hossain, M.F., Chen, W., Zhang, Y., 2015. Bulk density of mineral and organic soils in the Canada's arctic and sub-arctic. *Inform. Proc. Agric.* 2 (3–4), 183–190 doi:1016/j.inpa.2015.09.001.

Jin, M., Zheng, X., Jiang, T., Li, X., Li, X., Zhao, K., 2017. Evaluation and improvement of SMOS and SMAP soil moisture products for soils with high organic matter over a forested area in Northeast China. *Remote Sens.* 9 (4), 387 doi:3390/rs9040387.

Jones, S.B., Friedman, S.P., 2000. Particle shape effects on the effective permittivity of anisotropic or isotropic media consisting of aligned or randomly oriented ellipsoidal particles. *Water Resour. Res.* 36 (10), 2821–2833 doi:1029/2000WR900198.

Kasischke, E.S., Hayes, D.J., Billings, S., Boelman, N., Colt, S., Fisher, J., Wullschleger, S., 2014. A Concise Experiment Plan for the Arctic-Boreal Vulnerability Experiment. ORNL DAAC, Oak Ridge, TN, USA doi:3334/ORNLDAC/1617.

Kolka, R., Sebestyen, S., Verry, E.S., Brooks, K., 2011. Physical properties of organic soils. In: Brooks, K. (Ed.), *Peatland Biogeochemistry and watershed Hydrology at the Marcell Experimental Forest*. CRC Press, pp. 135–176 doi:1201/b10708-6.

Le Toan, T., Quegan, S., Davidson, M.W.J., Balzter, H., Paillou, P., Papathanassiou, K., Ulander, L., 2011. The BIOMASS mission: mapping global forest biomass to better understand the terrestrial carbon cycle. *Remote Sens. Environ.* 115 (11), 2850–2860 doi:1016/j.rse.2011.03.020.

Li, J., Zhao, S., Jiang, L., Chai, L., Wu, F., 2013, July. The influence of organic matter on soil dielectric constant at microwave frequencies (0.5–40 GHz). In: 2013 IEEE IGARSS (pp. 13–16). Doi:1109/IGARSS.2013.6721080.

Malicki, M.A., Plagge, R., Roth, C.H., 1996. Improving the calibration of dielectric TDR soil moisture determination taking into account the solid soil. *Eur. J. Soil Sci.* 47 (3), 357–366 doi:1111/j.1365-2389.1996.tb01409.x.

Manns, H.R., Berg, A.A., 2014. Importance of soil organic carbon on surface soil water content variability among agricultural fields. *J. Hydrol.* 516, 297–303 doi:1016/j.jhydrol.2013.11.018.

Matzler, C., Wegmuller, U., 1987. Dielectric properties of freshwater ice at microwave frequencies. *J. Phys. D. Appl. Phys.* 20 (12), 1623 doi:1088/0022-3727/20/12/013.

Miller, C.E., Griffith, P.C., Goetz, S.J., Hoy, E.E., Pinto, N., McCubbin, I.B., Margolis, H. A., 2019. An overview of ABoVE airborne campaign data acquisitions and science opportunities. *Environ. Res. Lett.* 14 (8), 080201 doi:1088/1748-9326/ab0d44.

Mironov, V., Savin, I., 2015. A temperature-dependent multi-relaxation spectroscopic dielectric model for thawed and frozen organic soil at 0.05–15 GHz. *Phys. Chem. Earth, Parts A/B/C* 83, 57–64 doi:1016/j.pce.2015.02.011.

Mironov, V.L., Dobson, M.C., Kaupp, V.H., Komarov, S.A., Kleshchenko, V.N., 2004. Generalized refractive mixing dielectric model for moist soils. *IEEE Trans. Geosci. Remote Sens.* 42 (4), 773–785 doi:1109/TGRS.2003.823288.

Mironov, V.L., De Roo, R.D., Savin, I.V., 2010. Temperature-dependable microwave dielectric model for an Arctic soil. *IEEE Trans. Geosci. Remote Sens.* 48 (6), 2544–2556 doi:1109/TGRS.2010.2040034.

Mironov, V.L., Kerr, Y.H., Kosolapova, L.G., Savin, I.V., Muzalevskiy, K.V., 2015. A temperature-dependent dielectric model for thawed and frozen organic soil at 1.4 GHz. *IEEE J. Select. Top. Appl. Earth Observ. Remote Sens.* 8 (9), 4470–4477 doi: 1109/JSTARS.2015.2442295.

Mironov, V.L., Kosolapova, L.G., Lukin, Y.I., Karavaysky, A.Y., Molostov, I.P., 2017. Temperature-and texture-dependent dielectric model for frozen and thawed mineral soils at a frequency of 1.4 GHz. *Remote Sens. Environ.* 200, 240–249 doi:1016/j.rse.2017.08.007.

Mironov, V.L., Kosolapova, L.G., Fomin, S.V., Savin, I.V., 2019. Experimental analysis and empirical model of the complex permittivity of five organic soils at 1.4 GHz in the temperature range from –30° C to 25° C. *IEEE Trans. Geosci. Remote Sens.* 57 (6), 3778–3787 doi:1109/TGRS.2018.2887117.

Mölders, N., Haferkorn, U., Döring, J., Kramm, G., 2003. Long-term investigations on the water budget quantities predicted by the hydro-thermodynamic soil vegetation scheme (HTSVS)—part I: description of the model and impact of long-wave radiation, roots, snow, and soil frost. *Meteorog. Atmos. Phys.* 84 (1), 115–135 doi:1007/s00703-002-0572-8.

Nicolksy, D.J., Romanovsky, V.E., Panteleev, G.G., 2009. Estimation of soil thermal properties using in-situ temperature measurements in the active layer and permafrost. *Cold Reg. Sci. Technol.* 55 (1), 120–129 doi:1016/j.coldregions.2008.03.003.

Niu, G.Y., Yang, Z.L., 2006. Effects of frozen soil on snowmelt runoff and soil water storage at a continental scale. *J. Hydrometeorol.* 7 (5), 937–952 doi:1109/JHM538.1.

Or, D., Wraith, J.M., 1999. Temperature effects on soil bulk dielectric permittivity measured by time domain reflectometry: a physical model. *Water Resour. Res.* 35 (2), 371–383 doi:1029/1998WR900008.

Park, C.H., Behrendt, A., LeDrew, E., Wulfmeyer, V., 2017. New approach for calculating the effective dielectric constant of the moist soil for microwaves. *Remote Sens.* 9 (7), 732 doi:3390/rs9070732.

Park, C.H., Montzka, C., Jagdhuber, T., Jonard, F., De Lanney, G., Hong, J., Wulfmeyer, V., 2019. A dielectric mixing model accounting for soil organic matter. *Vadose Zone J.* 18 (1) doi:2136/vzj/2019.04.0036.

Park, C.H., Berg, A., Cosh, M.H., Colliander, A., Behrendt, A., Manns, H., Wulfmeyer, V., 2021. An inverse dielectric mixing model at 50 MHz that considers soil organic carbon. *Hydrol. Earth Syst. Sci.* 25 (12), 6407–6420 doi:5194/hess-25-6407-2021.

Park, H., Kim, Y., Kimball, J.S., 2016. Widespread permafrost vulnerability and soil active layer increases over the high northern latitudes inferred from satellite remote sensing and process model assessments. *Remote Sens. Environ.* 175, 349–358 doi: 1016/j.rse.2015.12.046.

Peplinski, N.R., Ulaby, F.T., Dobson, M.C., 1995. Dielectric properties of soils in the 0.3–1.3-GHz range. *IEEE Trans. Geosci. Remote Sens.* 33 (3), 803–807 doi:1109/36.387598.

Petersen, L.W., Moldrup, P., Jacobsen, O.H., Rolston, D.E., 1996. Relations between specific surface area and soil physical and chemical properties. *Soil Sci.* 161 (1), 9–21.

Robinson, D.A., Friedman, S.P., 2001. Effect of particle size distribution on the effective dielectric permittivity of saturated granular media. *Water Resour. Res.* 37 (1), 33–40 doi:1029/2000WR900227.

Robinson, D.A., Jones, S.B., Blonquist, J.M., Heinse, R., Lebron, I., Doyle, T.E., 2009. The dielectric response of the tropical Hawaiian Mars soil simulant JSC Mars-1. *Soil Sci. Soc. Am. J.* 73 (4), 1113–1118 doi:2136/sssaj2008.0297.

Romanovsky, V.E., Osterkamp, T.E., 2000. Effects of unfrozen water on heat and mass transport processes in the active layer and permafrost. *Permafrost. Periglac. Process.* 11 (3), 219–239 doi:10.1002/1099-1530(200007/09)11:3%3C219:AID-PPP352%3E3.0.CO;2-7.

Rosen, P., Hensley, S., Shaffer, S., Edelstein, W., Kim, Y., Kumar, R., Sagi, R., 2017. The NASA-ISRO SAR (NISAR) mission dual-band radar instrument preliminary design. In: 2017 IEEE (IGARSS), pp. 3832–3835 doi:1109/IGARSS.2017.8127836.

Rosen, P.A., Hensley, S., Wheeler, K., Sadowsy, G., Miller, T., Shaffer, S., Madsen, S., 2006. UAVSAR: A new NASA airborne SAR system for science and technology research. In: 2006 IEEE Conference on Radar, p. 8 doi:1109/RADAR.2006.1631770.

Rowlandson, T.L., Berg, A.A., Bullock, P.R., Ojo, E.R., McNairn, H., Wiseman, G., Cosh, M.H., 2013. Evaluation of several calibration procedures for a portable soil moisture sensor. *J. Hydrol.* 498, 335–344 doi:1016/j.jhydrol.2013.05.021.

Savin, I., Mironov, V., Muzalevskiy, K., Fomin, S., Karavaysky, A., Ruzicka, Z., Lukin, Y., 2020. Dielectric database of organic Arctic soils (DDOAS). *Earth Syst. Sci. Data* 12 (4), 3481–3487 doi:5194/essd-12-3481-2020.

Savin, I.V., Muzalevskiy, K.V., Mironov, V.L., 2022. A dielectric model of thawed and frozen Arctic organic soils at 435 MHz. *Remote Sens. Lett.* 13 (5), 452–459 doi: 1080/2150704X.2022.2041761.

Schwartz, R.C., Evett, S.R., Pelletier, M.G., Bell, J.M., 2009a. Complex permittivity model for time domain reflectometry soil water content sensing: I. Theory. *Soil Sci. Soc. Am. J.* 73 (3), 886–897 doi:2136/sssaj2008.0194.

Schwartz, R.C., Evett, S.R., Bell, J.M., 2009b. Complex permittivity model for time domain reflectometry soil water content sensing: II. Calibration. *Soil Sci. Soc. Am. J.* 73 (3), 898–909 doi:2136/sssaj2008.0195.

Sihvola, A.H., Alanen, E., 1991. Studies of mixing formulae in the complex plane. *IEEE Trans. Geosci. Remote Sens.* 29 (4), 679–687 doi:1109/36.135831.

Smith, S.L., O'Neill, H.B., Isaksen, K., Noetzli, J., Romanovsky, V.E., 2022. The changing thermal state of permafrost. *Nat. Rev. Earth Environ.* 3 (1), 10–23 doi:1038/s43017-021-00240-1.

Stow, D.A., Hope, A., McGuire, D., Verbyla, D., Gamon, J., Huemmrich, F., Myneni, R., 2004. Remote sensing of vegetation and land-cover change in Arctic tundra ecosystems. *Remote Sens. Environ.* 89 (3), 281–308 doi:1016/j.rse.2003.10.018.

Tabatabaeenejad, A., Moghaddam, M., 2006. Bistatic scattering from three-dimensional layered rough surfaces. *IEEE Trans. Geosci. Remote Sens.* 44 (8), 2102–2114 doi: 1109/TGRS.2006.872140.

TEROS 12 manual, 2020. available at: http://publications.meter.group.com/Manuals/20587_TEROS11-12_Manual_Web.pdf.

TEROS, 2020. 21 Manual. available at: http://library.metergroup.com/Manuals/20854_TEROS21_Gen2_Manual_Web.pdf.

Topp, G.C., Davis, J.L., Annan, A.P., 1980. Electromagnetic determination of soil water content: measurements in coaxial transmission lines. *Water Resour. Res.* 16 (3), 574–582 doi:1029/WR016i003p00574.

Ulaby, F.T., El-Rayes, M.A., 1987. Microwave dielectric spectrum of vegetation-part II: dual-dispersion model. *IEEE Trans. Geosci. Remote Sens.* 5, 550–557 doi:1109/TGRS.1987.289833.

Ulaby, F.T., Bengal, T.H., Dobson, M.C., East, J.R., Garvin, J.B., Evans, D.L., 1990. Microwave dielectric properties of dry rocks. *IEEE Trans. Geosci. Remote Sens.* 28 (3), 325–336 doi:1109/36.54359.

Ulaby, F.T., Long, D.G., Blackwell, W.J., Elachi, C., Fung, A.K., Ruf, C., Van Zyl, J., 2014. Microwave Radar and Radiometric Remote Sensing, vol. 4, No. 5. University of Michigan Press, Ann Arbor, p. 6.

Wagner, N., Scheuermann, A., 2009. On the relationship between matric potential and dielectric properties of organic free soils: a sensitivity study. *Can. Geotech. J.* 46 (10), 1202–1215 doi:1139/T09-055.

Yang, F., Zhang, G.L., Yang, J.L., Li, D.C., Zhao, Y.G., Liu, F., Yang, F., 2014. Organic matter controls of soil water retention in an alpine grassland and its significance for hydrological processes. *J. Hydrol.* 519, 3086–3093 doi:1016/j.jhydrol.2014.10.054.

Yi, Y., Kimball, J.S., Chen, R.H., Moghaddam, M., Reichle, R.H., Mishra, U., Zona, D., Oechel, W.C., 2018. Characterizing permafrost active layer dynamics and sensitivity to landscape spatial heterogeneity in Alaska. *Cryosphere* 12 (1), 145–161 doi:5194/tc-12-145-2018.

Yi, Y., Chen, R.H., Kimball, J.S., Moghaddam, M., Xu, X., Euskirchen, E.S., Miller, C.E., 2022. Potential satellite monitoring of surface organic soil properties in Arctic tundra from SMAP. *Water Resour. Res.* 58 (4), e2021WR030957 doi:1029/2021WR030957.

Zona, D., Gioli, B., Commane, R., Lindaas, J., Wofsy, S.C., Miller, C.E., Oechel, W.C., 2016. Cold season emissions dominate the Arctic tundra methane budget. *Proc. Natl. Acad. Sci.* 113 (1), 40–45 doi:1073/pnas.1516017113.